SELF-ORDERING AND COLLECTIVE DYNAMICS OF TRANSVERSELY ILLUMINATED POINT-SCATTERERS IN A 1D TRAP

Masterarbeit

zur Erlangung des akademischen Grades
Master of Science (MSc)

an der
Fakultät für Mathematik, Informatik und Physik
der
Leopold-Franzens-Universität Innsbruck

vorgelegt von

Daniela Holzmann

Betreuer:
Univ.-Prof. Dr. Helmut Ritsch

Innsbruck, im Oktober 2014

The intellect has little to do on the road to discovery. There comes a leap in consciousness, call it intuition or what you will, and the solution comes to you and you don't know how or why.

Albert Einstein (1879-1955)

Abstract

We study the interaction and dynamics of a set of N particles along a 1D-nano-fibre coupled to the evanescent field of this fibre and additionally illuminated by a transversely coherent light. We use the transfer-matrix-method to calculate the field distribution and the optical forces acting on this system and look for equilibrium configurations. We solve the problem analytically for smaller particle numbers, concentrating on some special cases and derive conditions for self-consistent stable ordering. Afterwards we enlarge the system and examine the problem numerically, investigating the dynamics of the system. We discover that the particles form an equidistant lattice in the weak-scattering-limit with negligible back-scattering. For larger particle systems, the outermost particles tend to assemble near intensity maxima and trap light between them. At the end of this thesis we generalize the system to a geometry with directional asymmetric scattering. This introduces symmetry breaking and extra instabilities arise.

Zusammenfassung

Wir untersuchen die Wechselwirkung und Dynamik von N Teilchen, die mit einer 1D-Nanofaser gekoppelt sind. Diese Teilchen werden vom Evaneszenzfeld der Faser und zusätzlich von einem transversalen, kohärenten Licht bestrahlt. Mit Hilfe der Transfermatrix-Methode berechnen wir die Feldverteilung und die optischen Kräfte in einem solchen System und suchen nach Gleichgewichtskonfigurationen. Wir lösen das Problem für eine kleine Anzahl an Teilchen analytisch. Dabei konzentrieren wir uns auf einige Spezialfälle und erhalten Bedingungen für selbstkonsistente stabile Lösungen. Anschließend gehen wir für größere Systeme zu numerischen Lösungen über und untersuchen die Dynamik der Teilchen. Im Grenzfall für sehr schwache Streuung und vernachlässigbarer Rückstreuung ordnen sich die Teilchen zu einem äquidistanten Gitter an. Für eine größere Teilchenanzahl erhalten wir, dass die äußersten Teilchen sich neben einem Intensitätsmaxima anordnen und Licht dazwischen einfangen. Zum Schluss beziehen wir in unserem System gerichtete asymmetrische Streuung ein. Dadurch kommt es zu einer Symmetriebrechung und neue Instabilitäten tauchen auf.

Danksagung

Besonders bedanken möchte ich mich bei Univ.-Prof. Dr. Helmut Ritsch, der mir die Möglichkeit gab in seiner Forschungsgruppe zu arbeiten. Danke für das interessante Thema und für die tolle Zusammenarbeit in einer so netten Gruppe!

Bedanken möchte ich mich auch bei der gesamten Forschungsgruppe, die mich herzlich aufgenommen hat. Besonders erwähnen möchte ich dabei Matthias, der einen großen Beitrag zu meiner Masterarbeit geleistet hat und für das Gelingen mitverantwortlich ist. Du hattest immer Geduld und nahmst dir die Zeit Unklarheiten aus meinem Kopf zu schaffen! Für eure Hilfe bedanken, möchte ich mich auch bei Stefan, Tobias und Dominik, die mir bei Unsicherheiten meist erfolgreich weiterhelfen konnten. Bei Valentin und Sebastian möchte ich mich dafür bedanken, dass sie immer ein offenes Ohr für meine Fragen hatten.

Meiner gesamten Familie, die mich während des Studiums unterstützt hat, gilt ein besonderer Dank. Sowohl für die finanzielle, als auch für die persönliche Stütze möchte ich mich bei meinen Eltern bedanken, die während des gesamten Studiums immer an mich geglaubt haben. Erwähnen möchte ich auch meine zwei Brüder, Michael und Maximilian, die mir immer zur Seite stehen. Ein großes Dankeschön geht auch an meinen Freund Fabian, der mich nach allen Niederschlägen wieder aufgebaut hat und all die Jahre des Studiums unterstützt hat.

Auch möchte ich mich für die moralische Unterstützung bei all meinen Freunden bedanken, die mir halfen in der Freizeit meinen Kopf frei zu bekommen.

Contents

Chapter 1

Introduction

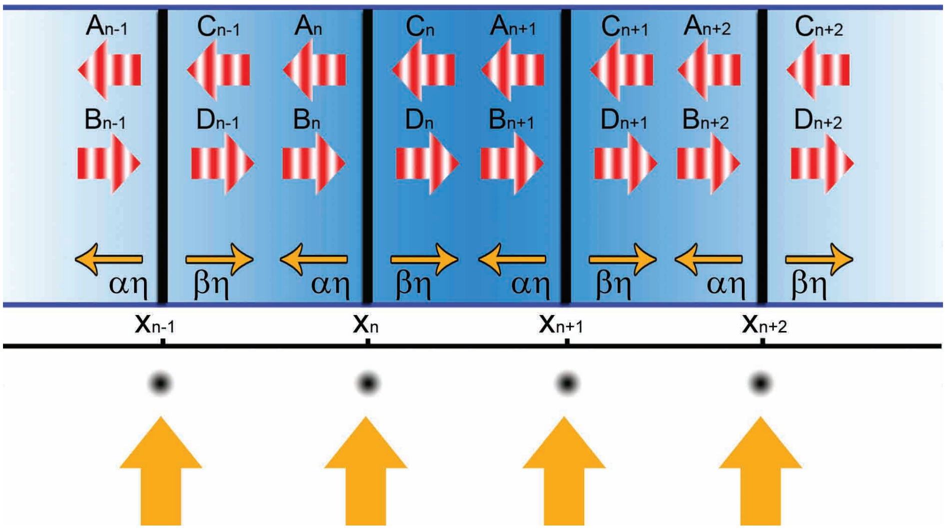

Figure 1.1: Particles confined in a 1D trap within the evanescent field of an optical nano-fibre are illuminated by two counter-propagating beams and a transverse pump. We treat the particles as beam-splitters interacting with a propagating wave in 1D. Hence we have two incoming fields from the left with amplitude B_1 and from the right C_N, the transverse pump η, and the outgoing fields to the left with amplitude A_1 and to the right D_N of the system. α and β correspond to the part of η scattered to the left and to the right.

Polarizable particles like atoms, nano-spheres, molecules, etc. that couple to confined light fields have been of rapidly growing interest for the past few years. One reason behind this rising interest is that such systems offer the possibility to control and manipulate single particles with high spatial precision.

In optical lattices particles are trapped by a standing wave composed of several laser beams forming a perfectly periodic lattice. The potentials created by optical lattices show periodic wells separated by half a wavelength of the incident laser light in the direction of incidence. Laser intensities and wavelengths may vary for different directions of incidence and therefore optical lattices are apt to study a huge variety of solid state lattice models [1].

They allow for investigation of eg. Bose-Hubbard Hamiltonian and its corresponding phase diagram [1], photonic band gaps [2] and quantum information science [3]. Laser-trapped atoms can be easily manipulated. They can be used in many ways, for example to probe atoms, molecules, quantum dots, and for mechanical manipulations [4]. For implementing quantum logic gates, neutral atoms are trapped in an optical lattice [3]. Optical lattice clocks use atoms trapped in an optical lattice as quantum time references [5].

In a common setup the lasers are far detuned from any resonance frequency, so that the dipole force dominates the scattering force, and the back-action from the particles on the laser light is small. Light scattering at particles shifts the laser wavelength and redistributes field energy among the incident laser beams. This generates interactions among the particles and may cause single and multi particle excitations as well as collective motion [2, 6–9].

The evanescent light field of optical nano-fibres allow for an optical lattice like field pattern along the surface of the fibre. In 2009/2010 Rauschenbeutel and coworkers [4] managed to trap laser-cooled neutral caesium atoms, interacting with the red- and blue-detuned evanescent field surrounding an optical nano-fibre (section 3.1). Optical nano-fibres permit trapping and optically interfacing neutral atoms. Rauschenbeutel's setup was improved with higher control of parameters and stronger particle-field coupling by other groups recently [10, 11]. In such highly confined fields back-scattering plays a dominant role in the system dynamics.

It is well established by now, that cold particles in optical resonators transversely illuminated by lasers undergo a phase transition from a homogeneous to regularly ordered phase at a sufficiently strong pump intensity and suitable detunings between laser and cavity field [12, 13]. The interactions in a 1D configuration for particles trapped along an optical nano-fibre illuminated by a Gaussian laser beam are examined in [14]. Chang [15] has investigated atoms coupled to a one-dimensional nano-photonic waveguide and driven identically by an external pump field, in the weak-scattering-limit.

The purpose of this work is to find self-consistent equilibrium solutions for N particle clouds along a 1D nano-fibre illuminated by a transverse pump field η. A scheme of our system is illustrated in Fig. 1.1. The particles can be trapped within the evanescent field of the fibre. Via coupling to the evanescent field of the fibre mode, the particles can scatter photons into and out of the two propagating light modes. The perturbation induced by the particles induces scattering between the incoming fields B_n and C_n and outgoing fields A_n and C_n. The transverse pump η illuminates all particles equally, which scatter the light into the fibre. By changing α and β, we can specify the part of η scattered to the left and to the right.

We start with an overview of the basic physics in chapter 2. Then we give a short introduction into the most important experimental setups (chapter 3). At the beginning we consider symmetric transverse scattering and examine the optical forces acting on a single particle (section 4.1). We concentrate on some special cases, and then slowly add more particles (section 4.2). In the multiparticle case we generally consider only transverse pump. Fist we solve the system analytically for smaller particle numbers and then pass over to larger systems and numerical solutions (section 4.3.2). As a special case we treat the weak-coupling-limit (section 4.3.1), where all the light is transmitted through the particles and no light is reflected. At the end of this work we take a short look at asymmetric scattering (chapter 5).

Chapter 2

Concepts and equations

To understand the basic methods used in this thesis, we first want to introduce the transfer-matrix-method. The transfer-matrix-method is used to describe the propagation of far detuned light through a lattice of single atom clouds. Light is considered as a plane wave with multiple scattering the particles represented by a set of beam-splitters [2, 6, 7, 16–18].

To understand this method, we first would like to introduce the basic equations of classical electrodynamics, the Maxwell's equations:

$$\nabla \cdot \mathbf{D} = \rho, \tag{2.1a}$$

$$\nabla \cdot \mathbf{B} = 0, \tag{2.1b}$$

$$\nabla \times \mathbf{E} = -\frac{\partial \mathbf{B}}{\partial t}, \tag{2.1c}$$

$$\nabla \times \mathbf{H} = \mathbf{J} + \frac{\partial \mathbf{D}}{\partial t}. \tag{2.1d}$$

Maxwell's equations relate electric and magnetic fields, $\mathbf{E}$ and $\mathbf{B}$, to the charge density ρ, the current density $\mathbf{J}$ and to induction, where the change of the magnetic field can induce an electric field and vice versa. The electric displacement $\mathbf{D} = \epsilon_0 \mathbf{E} + \mathbf{P}$, with the electric polarization $\mathbf{P}$ and the vacuum permittivity ϵ_0, and the magnetic field $\mathbf{H}$ defined via $\mathbf{B} = \mu \mathbf{H}$, with μ being the magnetic permeability, are needed for material media.

There we assume, that we have neutral particles with no electric charges $\rho = 0$ and no electric current $\mathbf{J} = 0$. [19, 20]

In the next sections we explain polarizability and introduce the inhomogeneous Helmholtz equation. With these we can understand the transfer-matrix-method and calculate the optical forces, which dominate the system.

2.1 Polarizabilities

An electrical field in dielectric media induces dipoles. The induced dipole moment per volume unit is called electrical polarization $\mathbf{P}(\mathbf{x})$. In a linear, homogeneous and isotropic media the polarization reads:

$$\mathbf{P}(\mathbf{x}) = \epsilon_0 \chi \mathbf{E}(\mathbf{x}) = \epsilon_0(\epsilon_r - 1)\mathbf{E}(\mathbf{x}), \tag{2.2}$$

with the electrical susceptibility $\chi = \epsilon_r - 1$.
The electrical field, that induces the polarization is the local field $\mathbf{E}_{loc}$ in the neighbourhood of the dipoles.
The whole dipole moment can be calculated by summing up the elementary dipole moments $\mathbf{d}_n \delta(\mathbf{x} - \mathbf{x}_n)$:

$$\mathbf{P}(\mathbf{x}) = \sum_{n=1}^{N} \mathbf{d}_n \delta(\mathbf{x} - \mathbf{x}_n) \approx N\mathbf{d}, \tag{2.3}$$

with the number of elementary dipoles per volume unit N. The average elementary dipole moment $\mathbf{d}$ is proportional to the local electrical field at the position of the dipole:

$$\mathbf{d}_n = \tilde{\alpha} \mathbf{E}_{loc}(\mathbf{x}_n), \tag{2.4}$$

with the polarizability $\tilde{\alpha}$. The origins of the polarizability are:

- The deformation of the electron shell because of the electrical field in non-polar material causes the polarizability $\tilde{\alpha}_{el}$.
- The shift of the ions in polar material leads to $\tilde{\alpha}_{ion}$.
- $\tilde{\alpha}_{orient}$ arises due to the orientation of the permanent dipoles in the outer field.

So the polarizability is: $\tilde{\alpha} = \tilde{\alpha}_{el} + \tilde{\alpha}_{ion} + \tilde{\alpha}_{orient}$.
The local field $\mathbf{E}_{loc}$ is composed of the macroscopic, outer field $\mathbf{E}$ and an additional field, which arises due to the polarization of the neighbouring dipoles. [21]
Also atoms can be polarized. Following [22] we get the linear polarizability tensor $\overset{\leftrightarrow}{\alpha}$ of a two-level quantum system in the dipole approximation, assuming that the size of an atom is much smaller than the wavelength of the radiation field and that the interaction between atom and radiation field is weak:

$$\overset{\leftrightarrow}{\alpha}(\omega) = \frac{\mathbf{d}_{12}\mathbf{d}_{21}}{\hbar} \left[\frac{1}{\omega_0 - \omega - i\gamma} + \frac{1}{\omega_0 + \omega + i\gamma} \right], \tag{2.5}$$

with the dipole matrix elements between the states $|m\rangle$ and $|n\rangle$ $\mathbf{d}_{mn} = \langle m|\mathbf{p}_a|n\rangle$, the electric dipole moment operator of the atom $\mathbf{p}_a = e\mathbf{r}$, the transition frequency $\omega_0 = (E_2 - E_1)/\hbar$, where E_n are the energy eigenvalues of the stationary states $|n\rangle$ and

the spontaneous decay rate $\gamma = 1/\tau$, with the average lifetime τ.
Assuming small values of γ, we can write Eq. (2.5) as follows:

$$\overset{\leftrightarrow}{\alpha}(\omega) = \frac{2\mathbf{d}_{12}\mathbf{d}_{21}}{\hbar}\left[\frac{\omega_0(\omega_0^2-\omega^2)}{(\omega_0^2-\omega^2)^2+4\gamma^2} + i\frac{2\gamma\omega\omega_0}{(\omega_0^2-\omega^2)^2+4\gamma^2}\right] = \Re(\alpha) + i\Im(\alpha). \tag{2.6}$$

As we will see later in this work, the real part of the polarizability is proportional to the dipole force and describes dispersive atom-light interactions, while the imaginary part is proportional to the radiation pressure and stands for dissipation. [6, 22]

2.2 Inhomogeneous Helmholtz equation in 1D

To derive the transfer-matrix-method we first have to understand the inhomogeneous Helmholtz equation in 1D.
At the beginning we calculate the curl of Eq. (2.1c):

$$\nabla \times (\nabla \times \mathbf{E}) + \frac{\partial}{\partial t}(\nabla \times \mathbf{B}) = \nabla \times (\nabla \times \mathbf{E}) + \mu_0 \frac{\partial}{\partial t}(\nabla \times \mathbf{H}) = 0. \tag{2.7}$$

Inserting Eq. (2.1d) and using $\nabla \times (\nabla \times \mathbf{E}) = \nabla(\nabla \cdot \mathbf{E}) - \nabla^2\mathbf{E} = -\Delta\mathbf{E}$, with $\nabla \cdot \mathbf{E} = 0$ as long as we have no free charges, we get:

$$-\Delta\mathbf{E} + \mu_0 \frac{\partial^2}{\partial t^2}\mathbf{D} = -\Delta\mathbf{E} + \mu_0\epsilon_0 \frac{\partial^2}{\partial t^2}\mathbf{E} + \mu_0 \frac{\partial^2}{\partial t^2}\mathbf{P} = 0. \tag{2.8}$$

Assuming the time-harmonic form $\mathbf{E}(\mathbf{x},t) = \mathbf{E}(\mathbf{x})\exp(-i\omega t)$, $\mathbf{D}(\mathbf{x},t) = \mathbf{D}(\mathbf{x})\exp(-i\omega t) = (\epsilon_0\mathbf{E}(\mathbf{x}) + \mathbf{P}(\mathbf{x}))\exp(-i\omega t)$ for all fields and defining $\epsilon_0\mu_0 = 1/c^2$, we obtain:

$$\Delta\mathbf{E} + \frac{\omega^2}{c^2}\mathbf{E} = -\mu_0\omega^2\mathbf{P}. \tag{2.9}$$

This is the inhomogeneous Helmholtz equation in 1D and describes the propagation of the electric field in dielectric media. [19]

2.3 Transfer-matrix-method

We use the inhomogeneous Helmholtz equation in 1D (2.9) to calculate the propagation of the electric field in dielectric media. To understand the transfer-matrix-method, we first consider only two counter-propagating laser beams of equal polarization and frequency, and afterwards we introduce an additional transverse light field (section. 2.3.1). We assume, that the transverse profile of the electric fields is Gaussian, with beam diameter much larger than the wavelength $\omega \gg \lambda$, so that the intensity maxima and minima are thin disks and we can substitute the laser light by plane waves. The

incident light from the left is $E(x,t) = E_0 \exp(ikx - i\omega t)$ and the one from the right $E(x,t) = E_1 \exp(-ikx - i\omega t)$ (Fig. 1.1). We drop the trivial phase factor $\exp(-i\omega t)$. The intensities can be calculated by $I_n(x) = 1/2\epsilon_0 c|E_n(x)|^2$, for $n \in 1, 2$. Additionally we assume linear polarizability for simplicity.
The particles can be „high-field seekers“ or „low-field seekers“. „High-field seekers“ are atoms with frequency ω_A larger than the laser light frequency ω_L, thus the trapping light is red detuned. This can also be submicron silica beads in a medium with lower index of refraction than that of the particles. These particles are pushed to the higher intensity. „Low-field seekers“ are cold particles, with blue detuned trapping light and they behave inversely to „high-field seekers“.
We average over transverse motion of particles in a cloud and assume, that this cloud is infinitely thin and of linear polarizable material. With Eq. (2.3), Eq. (2.4) and the density of the atom clouds $\rho = \tilde{\eta} \sum_{n=1}^{N} \delta(x - x_n)$, we obtain for the polarization density $P(x) = \tilde{\alpha}\tilde{\eta}E(x) \sum_{n=1}^{N} \delta(x - x_n)$ and the Helmholtz equation (2.9) in 1D for such N clouds looks as follows:

$$\left(\partial_x^2 + k^2\right) E(x) = -4\pi k^2 P = -4\pi k^2 \tilde{\eta}\tilde{\alpha} \sum_{n=1}^{N} \delta(x - x_n) E(x), \tag{2.10}$$

with surface density

$$\tilde{\eta} = \frac{N_\lambda}{\lambda^2} = \frac{\text{(number of particles in a cloud)}}{\text{(cloud cross section)}}, \tag{2.11}$$

linear polarizability $\tilde{\alpha}$, $k = \omega/c$ and the position of the n-th particle x_n. The strength of interaction between clouds and laser depends on the surface density and the linear polarizability. We define a coupling constant

$$\zeta = k\tilde{\eta}\frac{\tilde{\alpha}}{2\epsilon_0}, \tag{2.12}$$

the areal density of the polarizability of a cloud. This coupling constant is proportional to the forces acting on the particles. $\Re(\zeta)$ is proportional to the dipole force, which describes dispersive atom-light interactions and is positive for red detuning and negative for blue detuning. $\Im(\zeta)$ is always positive and describes dissipation like spontaneous emission. It is proportional to the radiation pressure force. Dipole and radiation pressure force are later described in detail.
With ζ, we can rewrite the Helmholtz equation (2.10):

$$\left(\partial_x^2 + k^2\right) E(x) = -2kE(x) \sum_{n=1}^{N} \zeta\delta(x - x_n). \tag{2.13}$$

The electric field between two clouds can be written as a superposition of two plane waves (see Fig. 1.1):

$$E(x_{n-1} < x < x_n) = A_n e^{-ik(x-x_n)} + B_n e^{ik(x-x_n)} = C_{n-1} e^{-ik(x-x_{n-1})} + D_{n-1} e^{ik(x-x_{n-1})}. \tag{2.14}$$

The electric field has to fulfil some boundary conditions. First it has to be continuous at the infinitely thin cloud:

$$E(x_n - 0) = E(x_n + 0). \tag{2.15}$$

From Eq. (2.13) we can find boundary conditions for the derivative of the fields. We integrate Eq. (2.13) from $x_n - \epsilon$ to $x_n + \epsilon$, with $\epsilon \to 0$, and we get:

$$\begin{aligned}
&\int_{x_n-\epsilon}^{x_n+\epsilon} \left(\partial_x^2 + k^2\right) E(x) = \int_{x_n-\epsilon}^{x_n+\epsilon} -2kE(x) \sum_{j=1}^{N} \zeta \delta(x - x_j), \\
&\partial_x E(x_n - 0) - \partial_x E(x_n + 0) + k^2(E(x_n - 0) - E(x_n + 0)) = -2k\zeta E(x_n), \\
&\partial_x E(x_n - 0) = \partial_x E(x_n + 0) + 2k\zeta E(x_n),
\end{aligned} \tag{2.16}$$

where we used Eq. (2.15) in the last line. The boundary conditions (2.15) and (2.16) connect the amplitudes to the right of each atom cloud with those to the left. Inserting Eq. (2.14) in Eq. (2.15), we get the following boundary condition for our system:

$$A_n + B_n = C_n + D_n. \tag{2.17}$$

Using this equation, we get from Eq. (2.16):

$$\begin{aligned}
-iA_n + iB_n &= -iC_n + iD_n + 2\zeta(A_n + B_n), \\
-iA_n &= -iC_n + \zeta(A_n + B_n), \\
A_n &= \frac{i\zeta}{1 - i\zeta} B_n + \frac{1}{1 - i\zeta} C_n,
\end{aligned} \tag{2.18}$$

and

$$\begin{aligned}
-iA_n + iB_n &= -iC_n + iD_n + 2\zeta(C_n + D_n), \\
iB_n &= iD_n + \zeta(C_n + D_n), \\
D_n &= \frac{1}{1 - i\zeta} B_n + \frac{i\zeta}{1 - i\zeta}.
\end{aligned} \tag{2.19}$$

An electric field propagating in the x-direction, $E_{inc} = E_0 \exp(ikx)$ is split into a reflected $E_{ref} = rE_0 \exp(-ikx)$ and a transmitted field $E_{trans} = tE_0 \exp(ikx)$, when

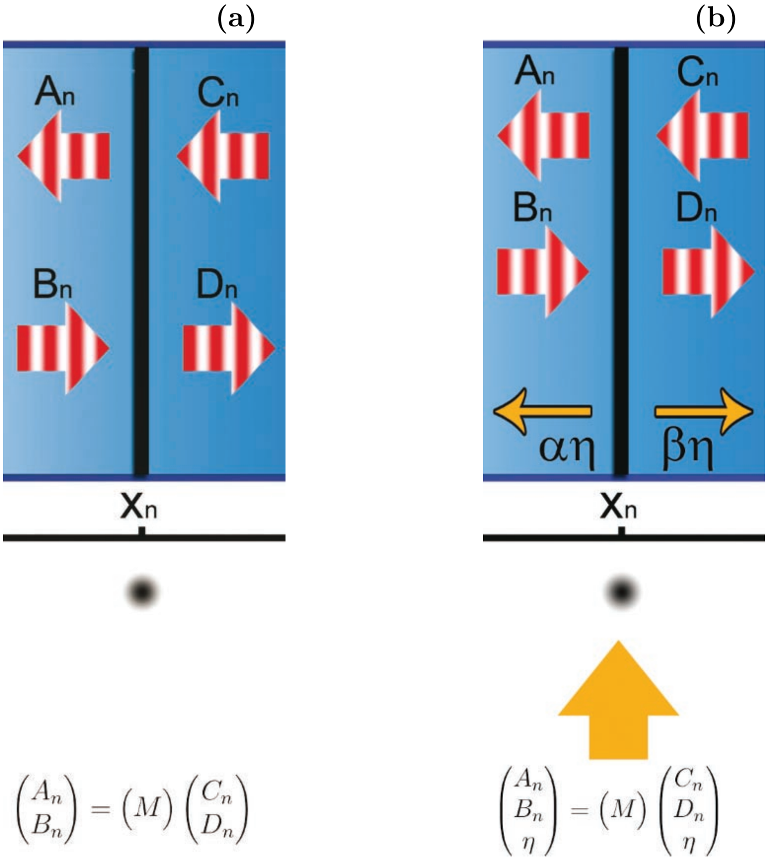

$$\begin{pmatrix} A_n \\ B_n \end{pmatrix} = (M) \begin{pmatrix} C_n \\ D_n \end{pmatrix}$$

$$\begin{pmatrix} A_n \\ B_n \\ \eta \end{pmatrix} = (M) \begin{pmatrix} C_n \\ D_n \\ \eta \end{pmatrix}$$

Figure 2.1: The transfer-matrix-method with two longitudinal fields (a) and additional transverse pump (b). B_n and C_n are the incoming amplitudes, while A_n and D_n are the outgoing ones. The transfer-matrix-method relates the modes to the left of an optical element to the modes to the right of it.

colliding on a beam-splitter, with reflection r and transmission coefficient t. So the boundary conditions (2.18) and (2.19) change into:

$$A_n = rB_n + tC_n, \tag{2.20}$$

$$D_n = tB_n + rC_n. \tag{2.21}$$

Comparing Eq. (2.20) with Eq. (2.18) and Eq. (2.19), we can rewrite the reflection and transmission coefficient in the following way:

$$r = \frac{i\zeta}{1 - i\zeta}, \tag{2.22}$$

$$t = \frac{1}{1 - i\zeta}, \tag{2.23}$$

with $\zeta = -ir/t$. Reflection and transmission coefficient are related to each other in the following way: $|r|^2 + |t|^2 = 1 - 2|t|^2\Im(\zeta)$ and $r + 1 = t$.

With these relations for a single beam-splitter, we are now able to describe a set of N particle clouds as a set of N beam-splitters. To do this we use the transfer-matrix-method. Up to now, we have related the outgoing modes to the incoming modes. The transfer-matrix-method relates the modes to the left of an optical element to the modes to the right of it, as we can see in Fig. 2.1a):

$$\begin{pmatrix} A_n \\ B_n \end{pmatrix} = \begin{pmatrix} M \end{pmatrix} \begin{pmatrix} C_n \\ D_n \end{pmatrix} \tag{2.24}$$

We define the incoming field amplitudes $E_0 = B_1$ and $E_1 = C_N$ and the outgoing field amplitudes are A_1 and D_N. Reordering Eq. (2.20) and Eq. (2.21), we can write the amplitudes to the left of one optical element as:

$$A_n = \frac{1}{t}\Big((t^2 - r^2)C_n + rD_n\Big) = (1 + i\zeta)C_n + i\zeta D_n, \tag{2.25}$$

$$B_n = \frac{1}{t}\left(-rC_n + D_n\right) = -i\zeta C_n + (1 - i\zeta)D_n. \tag{2.26}$$

So the matrix for one beam-splitter looks as follows:

$$M_{BS} = \frac{1}{t}\begin{pmatrix} t^2 - r^2 & r \\ -r & 1 \end{pmatrix} = \begin{pmatrix} 1 + i\zeta & i\zeta \\ -i\zeta & 1 - i\zeta \end{pmatrix}. \tag{2.27}$$

For a set of more beam-splitters we have to consider the propagation of light, between two beam-splitters. Although the intensity does not change, the amplitudes can acquire phases. The following matrix $P(d)$ includes the propagation of light:

$$P(d) = \begin{pmatrix} e^{ikd} & 0 \\ 0 & e^{-ikd} \end{pmatrix}, \tag{2.28}$$

with d the distance between the two beam-splitters.

Now we can easily calculate the transfer-matrix of the whole system. This matrix can be calculated by multiplying the matrices of the single beam-splitters and the propagation matrix:

$$\begin{aligned} M &= M_{BS} \cdot P(d_1) \cdot M_{BS} \cdot P(d_2) \cdot M_{BS} \cdots M_{BS} \cdot P(d_{N-1}) \cdot M_{BS} \\ &= \frac{1}{T_l}\begin{pmatrix} T_lT_r - R_lR_r & R_l \\ -R_r & 1 \end{pmatrix}, \end{aligned} \tag{2.29}$$

with R and T being the reflection and transmission coefficient to the left l or to the right r side of the whole system and defined via $A_1 = R_lB_1 + T_rC_N$ and $D_N = R_rC_N + T_lB_1$. While for one beam-splitter $R_l = R_r$, the reflection coefficient for left

and right incoming light usually do not coincide for more particles. The transmission amplitude is independent of the direction of propagation and so $T_l = T_r$ [7].
As we can see in [7] the group of transfer matrices $(\mathcal{T}, \cdot)$ can be defined as:

$$\mathcal{T} = \{T \in \mathbb{C}^{2\times 2} | \exists r_1, r_2, t \in \mathbb{C} : T = \frac{1}{t}\begin{pmatrix} t^2 - r_1 r_2 & r_2 \\ -r_1 & 1 \end{pmatrix} \equiv T(r_1, r_2, t)\}, \tag{2.30}$$

with $T_1 \cdot T_2 \in \mathcal{T}$ for all $T_1, T_2 \in \mathcal{T}$ and $[T(r_1, r_2, t)]^{-1} \in \mathcal{T}$.
So we found the transfer-matrix of a set of N beam-splitters with two incoming counter-propagating laser fields. [2, 6, 7, 16, 17]
In the next section, we want to apply this formalism on our system with two counter-propagating longitudinal laser fields and one transverse pump, and find a transfer-matrix for this system.

2.3.1 Transfer-matrix-method with transverse laser

As shown in Fig. 2.1b), for this system we have to add the scattered fields to the propagation and hence the outgoing amplitudes look as follows:

$$A_n = rB_n + tC_n + \alpha\eta, \tag{2.31}$$
$$D_n = tB_n + rC_n + \beta\eta, \tag{2.32}$$

with α the part of η reflected to the left and β the one reflected to the right. α and β fulfil the condition $|\alpha|^2 + |\beta|^2 = 1$, so that we later write $\alpha = \sin(\theta)$ and $\beta = \cos(\theta)$. Using Fermi's golden rule [4, 23, 24], we get that the decay rate γ into the fibre is proportional to $|\mathbf{d} \cdot \mathbf{E}_{loc}|^2$, with the dipole moment $\mathbf{d}$. As $\mathbf{d} = \tilde{\alpha}\mathbf{E}_{loc}$ (Eq. (2.4)) and $\gamma \propto I_\eta = c\epsilon_0/2|\eta|^2$, it follows $\eta \propto \tilde{\alpha}\mathbf{E}_{loc}^2$.
While the fibre and the laser pump are translation and mirror symmetric and one expects $\alpha = \beta$, this is not true due to polarization of the pump. This was shown recently by [25].
We can rewrite Eq. (2.31) and Eq. (2.32), so that we relate the amplitudes to the left of the optical element to the ones to the right of it:

$$A_n = \frac{1}{t}\Big((t^2 - r^2)C_n + rD_n + (\alpha t - \beta r)\eta\Big) = (1 + i\zeta)C_n + i\zeta D_n + (\alpha - i\beta\zeta)\eta, \tag{2.33}$$
$$B_n = \frac{1}{t}\left(-rC_n + D_n - \beta\eta\right) = -i\zeta C_n + (1 - i\zeta)D_n + \beta(i\zeta - 1)\eta. \tag{2.34}$$

The transfer-matrix M in this case is a 3×3-matrix, and defined via:

$$\begin{pmatrix} A_n \\ B_n \\ \eta \end{pmatrix} = \Big(M\Big) \begin{pmatrix} C_n \\ D_n \\ \eta \end{pmatrix}, \tag{2.35}$$

and looks as follows:

$$M_{BS} = \frac{1}{t}\begin{pmatrix} t^2 - r^2 & r & \alpha t - \beta r \\ -r & 1 & -\beta \\ 0 & 0 & t \end{pmatrix} = \begin{pmatrix} 1 + i\zeta & i\zeta & \alpha - i\beta\zeta \\ -i\zeta & 1 - i\zeta & \beta(i\zeta - 1) \\ 0 & 0 & 1 \end{pmatrix}. \tag{2.36}$$

As for the transfer-matrix without the transverse pump, we define the set of transfer matrices as:

$$\mathcal{T} = \{T \in \mathbb{C}^{2\times 2} | \exists r_1, r_2, t \in \mathbb{C} : T = \frac{1}{t}\begin{pmatrix} t^2 - r^2 & r & \alpha t - \beta r \\ -r & 1 & -\beta \\ 0 & 0 & t \end{pmatrix} \equiv T(r_1, r_2, t)\}, \tag{2.37}$$

Since $M_{BS_1} \cdot M_{BS_2} \in \mathcal{T}$ and $[M_{BS}]^{-1} \in \mathcal{T}$, $(\mathcal{T}, \cdot)$ is a group with the standard matrix multiplication $(\cdot)$.
So we found the transfer-matrix for a system with two counter-propagating longitudinal and one transverse laser field.
For this case the propagation matrix looks as follows:

$$P(d) = \begin{pmatrix} e^{ikd} & 0 & 0 \\ 0 & e^{-ikd} & 0 \\ 0 & 0 & 1 \end{pmatrix}. \tag{2.38}$$

As already seen in Eq. (2.29) the approach of this method is to find a matrix, which consists of matrix products of the beam-splitter and the propagation matrix, and connects the amplitudes to the left of the system with those to the right of it:

$$M = M_{BS} \cdot P(d_1) \cdot M_{BS} \cdot P(d_2) \cdot M_{BS} \cdots M_{BS} \cdot P(d_{N-1}) \cdot M_{BS}. \tag{2.39}$$

2.4 Optical forces

As the particles redistribute the light, they change its momentum and thus experience a light force. To find the equilibrium positions of the particles in our system, we have to calculate these forces acting on the system. Usually in free space the radiative force on atoms at rest can be separated into two parts [26]:

- Radiation pressure: connected to the phase gradient of the laser
- Dipole force: connected to the intensity gradient of the laser

The force on a dipole in an electrical field $E(x)$ reads [27]:

$$F = \frac{1}{4}\frac{\partial}{\partial_x}|E(x_0)|^2 \Re(\tilde{\alpha}) - \frac{1}{2}|E(x_0)|^2 \frac{\partial}{\partial_x}\phi(x_0)\Im(\tilde{\alpha}), \tag{2.40}$$

with x_0 the position of the dipole, $\tilde{\alpha}$ the polarizability of the dipole and $E(x) = |E(x)| \exp(-i\phi(x))$. The term proportional to the real part of the polarizability $\tilde{\alpha}$ is called dipole or gradient force and the term proportional to $\Im(\alpha)$ radiation pressure or scattering force.
For our system, we require far detuned lasers, so that the dipole force dominates the scattering force, the light does not heat the particles very much and the optical back-action of the particles on the light is very small. [6]

2.4.1 Dipole force

The electric field induces an oscillating dipole in an atom, which again interacts with the field. The spatial gradient of the strength of this interaction leads to the dipole force, sometimes also called gradient force. As we can see in Eq. (2.40), for a stationary particle it is proportional to the gradient of the intensity [28]. Because of the dipole force, particles with $\Re(\zeta) > 0$ are pushed toward high intensities, and particles with $\Re(\zeta) < 0$ toward lower intensities. [6]
There are different possibilities to understand the basic physics of the dipole force [29]:

- The dipole force can be associated to a driven oscillator. The charge, driven by the electric field, is in phase with the field, when the light is red detuned ($\omega_L < \omega_A$), and 180° out of phase, when the light is blue detuned. The interaction energy between the induced dipole $\mathbf{p} = \tilde{\alpha}\mathbf{E}$ and the field is $U_{dip} = -\mathbf{pE} = \tilde{\alpha}|\mathbf{E}|^2$. We can see that the interaction energy is negative for red detuned light and the oscillator is pushed toward higher intensities to minimize the energy. For blue detuned light the interaction energy is positive and the oscillator pushed toward lower intensities.

- The second possibility to describe the dipole force is as a consequence of absorption and stimulated emission. It arises due to photon absorption from one wave followed by stimulated emission into another one. The energy of the field does not change, because all waves have the same frequency. However, as the single waves have different $\mathbf{k}$-vectors, the photon impulses are redistributed and thus also the momentum of the atoms changes. [26]

2.4.2 Radiation Pressure

In contrast to the dipole force, the radiation pressure is a consequence of absorption and spontaneous emission. It arises from the momentum transmitted to the atom, when spontaneously scattering a photon into a random direction. A photon with momentum $\hbar\mathbf{k}$ totally absorbed by an atom with initial antiparallel $\mathbf{v}_i$, final velocity $\mathbf{v}_f$ and mass M transmits the following recoil velocity: $\mathbf{v}_R = \mathbf{v}_i - \mathbf{v}_f = \hbar\mathbf{k}/M$. Then the atom emits the photon in a random direction as we can see in Fig. 2.2. So the atom absorbs photons only

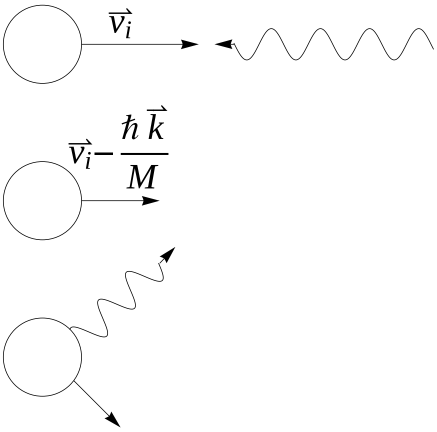

Figure 2.2: An atom, scattering a photon, that transmits a momentum to the atom. First, the atom absorbs the photon, propagating antiparallel to it, which transmits its momentum to it and slow down the atom. Then the atom emits the photon in a random direction.

from one direction, but emits them in every possible direction. So only the part from absorption contributes to the average. For two incoming fields the radiation pressure force is proportional to the difference of the intensity between the two longitudinal incoming laser fields and points toward the weaker source. The force fluctuates in time, due to the fact, that direction and time of emission are statistically distributed, which leads to diffusion of the atomic motion in the momentum space. [6, 29]

2.4.3 Maxwell stress tensor

The theory of the electromagnetic forces is based on the conservation of momentum. Recalling Maxwell's equations, we calculate the Maxwell stress tensor. Operating on Eq. (2.1c) by $\times\epsilon_0\mathbf{E}$ and on Eq. (2.1d) by $\times\mu_0\mathbf{H}$, and adding this two equations, we get:

$$\epsilon_0(\nabla \times \mathbf{E}) \times \mathbf{E} + \mu_0(\nabla \times \mathbf{H}) \times \mathbf{H} = -\frac{1}{c^2}\left(\frac{\partial \mathbf{H}}{\partial t} \times \mathbf{E}\right) + \frac{1}{c^2}\left(\frac{\partial \mathbf{E}}{\partial t} \times \mathbf{H}\right), \tag{2.41}$$

with $\epsilon_0\mu_0 = 1/c^2$. Using Eq. (2.1a), we can write the first two expressions in the following way:

$$\epsilon_0(\nabla \times \mathbf{E}) \times \mathbf{E} = \nabla\left(\epsilon_0\mathbf{E}\cdot\mathbf{E} - \frac{\epsilon_0}{2}E^2\mathbb{1}\right) - \epsilon_0\mathbf{E}\nabla\mathbf{E} = \nabla\left(\epsilon_0\mathbf{E}\cdot\mathbf{E} - \frac{\epsilon_0}{2}E^2\mathbb{1}\right) - \rho\mathbf{E}, \tag{2.42}$$

and using Eq. (2.1b):

$$\mu_0(\nabla \times \mathbf{H}) \times \mathbf{H} = \nabla\left(\mu_0\mathbf{H}\cdot\mathbf{H} - \frac{\mu_0}{2}H^2\mathbb{1}\right). \tag{2.43}$$

With

$$\frac{1}{c^2}\frac{d}{dt}\left(\mathbf{E}\times\mathbf{H}\right)=\frac{1}{c^2}\left(\frac{\partial\mathbf{E}}{\partial t}\times\mathbf{H}\right)-\frac{1}{c^2}\left(\frac{\partial\mathbf{H}}{\partial t}\times\mathbf{E}\right), \tag{2.44}$$

we get:

$$\nabla\left(\epsilon_0\mathbf{E}\cdot\mathbf{E}+\mu_0\mathbf{H}\cdot\mathbf{H}-\frac{1}{2}\left(\epsilon_0 E^2+\mu_0 H^2\right)\mathbb{1}\right)=\frac{d}{dt}\frac{1}{c^2}\left(\mathbf{E}\times\mathbf{H}\right). \tag{2.45}$$

In this way we arrived at Maxwell's stress tensor in vacuum $\overset{\leftrightarrow}{\mathbf{T}}$, which is defined as:

$$\overset{\leftrightarrow}{\mathbf{T}}=\epsilon_0\mathbf{E}\cdot\mathbf{E}+\mu_0\mathbf{H}\cdot\mathbf{H}-\frac{1}{2}\left(\epsilon_0 E^2+\mu_0 H^2\right)\mathbb{1}. \tag{2.46}$$

From Poynting's theorem follows that the total force onto an object in an electromagnetic field is the sum of the mechanical and the field force:

$$\begin{aligned}\mathbf{F}=&\mathbf{F}_{mech}+\mathbf{F}_{field}=\int_V\left(\rho\mathbf{E}+\frac{1}{c}\mathbf{J}\times\mathbf{B}\right)dV+\frac{1}{c^2}\int_V\frac{d}{dt}\left(\mathbf{E}\times\mathbf{H}\right)dV\\=&\epsilon_0\int_V\frac{d}{dt}\left(\mathbf{E}\times\mathbf{B}\right)dV.\end{aligned} \tag{2.47}$$

So we first have to integrate Eq. (2.45) over an arbitrary volume V:

$$\int_V\nabla\overset{\leftrightarrow}{\mathbf{T}}\,dV=\frac{d}{dt}\frac{1}{c^2}\int_V\left(\mathbf{E}\times\mathbf{H}\right)dV. \tag{2.48}$$

Using Gauss' integration law $\int_V\overset{\leftrightarrow}{\mathbf{T}}\,dV=\int_{\partial V}\overset{\leftrightarrow}{\mathbf{T}}\cdot\mathbf{n}\,da$, with ∂V the surface of V, $\mathbf{n}$ the unit vector perpendicular to the surface and da an infinitesimal surface element, we can transform the volume integral into a surface integral, and obtain:

$$\mathbf{F}=\int_{\partial V}\overset{\leftrightarrow}{\mathbf{T}}\cdot\mathbf{n}\,da. \tag{2.49}$$

Now we can calculate the mechanical force acting on an arbitrary body within the closed surface ∂V. It is interesting to see that the force only depends on the electromagnetic fields $\mathbf{E}$ and $\mathbf{B}$. For our one-dimensional problem, we are only interested in the x-component of the Maxwell stress tensor. Assuming vacuum, we get [19, 22]:

$$T_{xx}=\frac{\epsilon_0}{2}\left(E_x^2-E_y^2-E_z^2+c^2(B_x^2-B_y^2-B_z^2)\right). \tag{2.50}$$

Considering the facts, that the electric and magnetic fields are always orthogonal to the propagation direction x, thus $E_x=B_x=0$, and that electromagnetic waves are transversal $|c\mathbf{B}|=|\mathbf{E}|$, the Maxwell stress tensor changes into [16]:

$$\overset{\leftrightarrow}{\mathbf{T}}=-\epsilon_0\mathbf{E}^2. \tag{2.51}$$

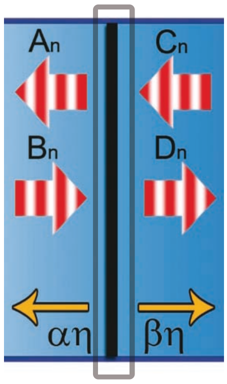

Figure 2.3: We integrate over the momentum flux on the boundaries of the fictitious box (grey rectangular). For our infinitely thin beam-splitters, the length of this box parallel to the x-axis is infinitesimally small and does not influence our integral. So we only have to integrate over the two planes orthogonal to the x-axis.

To calculate the force on our system, we now can enclose the body in a fictitious box and integrate over the boundary of it as we can see in Fig. 2.3. For our system the planes parallel to the x-axis are infinitesimally small, so we only have to take into account the planes orthogonal to the x-axis. Inserting this in Eq. (2.49) and integrating over the surface, we get the force on the n-th-beam-splitter:

$$F_n = \frac{\epsilon_0}{2}\left(|A_n|^2 + |B_n|^2 - |C_n|^2 - |D_n|^2\right). \tag{2.52}$$

It is easy to see, that the force corresponds to the missing momentum, which leads to a force on the inner volume. The part $|A|^2 - |C|^2$ are the missing photons coming from the right, which leads to a force toward the right direction, while the part $-(|D|^2 - |B|^2)$ shows the missing photons coming from the left, which leads to a force toward the left direction.

For only longitudinal incoming laser light with amplitudes $B(x) = \sqrt{2I_l/(\epsilon_0 c)}\exp(ik(x-x_0)+i\phi_B)$ and $C(x) = \sqrt{2I_r/(\epsilon_0 c)}\exp(-ik(x-x_0)+i\phi_C)$, the force, Eq. (2.52), on one beam-splitter reads:

$$\begin{aligned} F =& \frac{\epsilon_0}{2}\left(|A|^2 + |B|^2 - |C|^2 - |D|^2\right), \\ =& \frac{\epsilon_0}{2}\left(|(1+i\zeta)C + i\zeta D|^2 + |-i\zeta C + (1-i\zeta)D|^2 - |C|^2 - |D|^2\right), \\ =& \underbrace{\frac{2(I_l - I_r)\zeta_i}{c|1-i\zeta|^2}}_{A} - \underbrace{\frac{4\sqrt{I_l I_r}\zeta_r\sin(2kx))}{c|1-i\zeta|^2}}_{B} + \underbrace{\frac{2(I_l - I_r)\,|\zeta|^2}{c|1-i\zeta|^2}}_{C}, \end{aligned} \tag{2.53}$$

where we have chosen $x_0 = (\phi_B - \phi_C)/2k$. Term A is proportional to the imaginary part of ζ and a part of the radiation pressure, arising due to absorption of photons. It is also proportional to the difference of the intensity of the two incoming laser fields and points toward the weaker force. It vanishes for $I_l = I_r$. The interference term B corresponds to the dipole force and is proportional to the real part of ζ. For $\Re(\zeta) > 0$ it points toward high intensities and for $\Re(\zeta) < 0$ vice versa. It arises due to redistribution of photons between the light waves. The last term C is proportional to $|\zeta|^2$ and thus very small for one particle. It corresponds to reflection without considering effects of interference. The factor $|1 - \zeta|^2$ reduces the force because of the presence of the beam-splitter. [6]

Chapter 3

Implementation examples

Before we start with the main part of this work, we want to give a short overview of the possible realization methods for the system. The main requirements are to couple emitters to guided field modes to trap dipoles in 1D. Two types of optical fibres have been developed to couple small particles with light. While in hollow-core fibres the atoms are injected with a capillary into the centre of the fibre, in optical nano-fibres with the diameter smaller than the wavelength of the guided light, the particles are positioned along the fibre and interact with the evanescent field of the fibre.

Optical waveguides in the form of glass fibres have a higher refractive index core and a lower index cladding, which causes total reflection at the boundary. Nevertheless an evanescent field rises in the cladding [25]. The fibre or V-Parameter $V = 2\pi a/\lambda NA$ shows the number of modes of the fibre. $NA = \sqrt{n_1^2 - n_2^2}$ stands for the numerical aperture of the fibre, with n_1 and n_2 the refractive indices of the core and the cladding, a the radius of the core, and λ the wavelength of the light in the fibre. The number M of modes in the fibre is approximately $M \approx 4V^2/\pi^2$ for $V \gg 1$. For a single mode fibre is $V < 2.405$. [30]

A subwavelength-diameter fibre can be prepared by using taper fibre technology. A single-mode optical fibre is heated and pulled to a very thin thickness. Due to this, the fibre core is almost vanishing and the significant refractive indices are the one of the clad and the one of the surrounding vacuum. The fibre core can be neglected and the light is guided along the interface between the cladding and the surrounding media, instead of along the interface between the core and the cladding. In such waveguides the penetration length of the evanescent field is much larger than the diameter of the fibre. [31, 32]

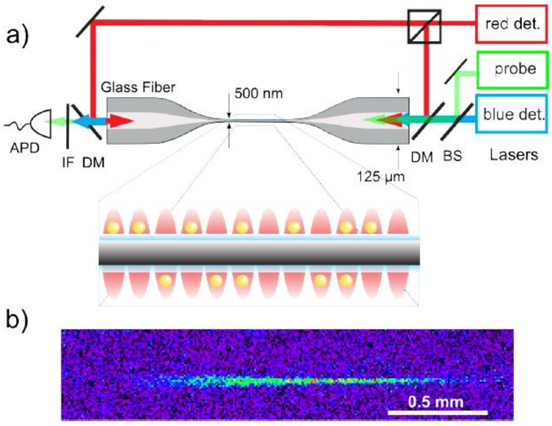

Figure 3.1: Fig. a) demonstrates the experimental setup to trap atoms in the evanescent field surrounding an optical nano-fibre. Two counter-propagating waves, one blue and the other red detuned, create the trapping potential. An additional resonant laser probes the atoms via the evanescent field.
Fig. b) shows the fluorescence image of this ensemble. [4]

3.1 Optical interface created by laser-cooled atoms trapped in the evanescent field surrounding an optical nano-fibre

Rauschenbeutel and coworkers [4] managed to trap and optically interface laser-cooled neutral caesium-atoms in a one-dimensional optical lattice about 200 nm above the nano-fibre surface. They positioned the atoms along a nano-fibre with diameter much smaller than the wavelength of the guided light. The guided light in this nano-fibre can penetrate into the surrounding media, so that particles along the fibre can interact with this evanescent field, by absorbing light from the fibre or emitting light into the fibre. The intensity of the evanescent field as a function of the distance x from the surface is given by $I(x) = I_0 \exp(-2x/\Lambda)$, with the decay length Λ, where $I(x) \propto 1/e^2$ and I_0 the intensity at the surface [33, 34].
The experimental setup is sketched in Fig. 3.1. A 500 nm diameter nano-fibre with red- and blue-detuned evanescent light field around this fibre is inserted into a magneto-optical trap. Such a fibre only guides the fundamental HE_{11} mode, which can be pumped simultaneously with different lasers. While the red-detuned light and the Van-der-Waals-force attract the atoms toward the nano-fibre, the blue-detuned light pushes them away. A potential minimum is then created, because of the faster radial decay lengths of the blue-detuned evanescent fields in comparison to red light. To fix the atoms in the axial direction, a backward-propagating red-detuned standing wave is additionally sent through the fibre. [35]

Higher order modes of a nano-fibre leads to a higher evanescent field and thus to a stronger interaction with the atoms [36]. Such fibres are called few-mode optical nano-fibres. The interaction of ^{87}Rb with such nano-fibres are investigated in [37].

3.2 High-cooperativity nano-fibre laser

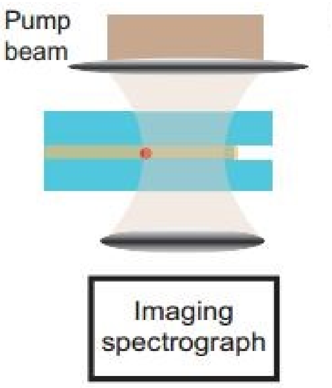

Figure 3.2: In this setup the capillaries are pumped from the side with a low-NA lens. [38]

Another experimental setup is shown in Fig. 3.2, where was tried to couple gold nano-particles to a highly confined mode of a nano-fibre without use of any cavity geometry. First they filled gold nano-particles into a capillary and then phenol, and pumped it from the side with a cigar-shaped beam. A grating and a camera was used to measure the emission spectrum along the fibre. This system was even operated as a laser. [38]

3.3 Exploiting the local polarization of strongly confined light for sub-micron-resolution internal state preparation and manipulation of cold atoms

An experimental setup to manipulate atomic ensembles by a single optical mode, that exhibits a local polarization, is shown in [39]. With the same experimental setup introduced by Rauschenbeutel [4], they managed to manipulate two distinct atomic ensembles with a single laser field. They prepared the two ensembles in two opposite Zeeman states, thus, the ensembles interact differently with a single mode light field. The experimental setup is shown in Fig. 3.3. Caesium atoms are trapped along the evanescent field of a nano-fibre. Two diametric arrays of individual trapping sites are created by a red-detuned standing and a blue-detuned running wave. The only guided mode by the nano-fibre is the fundamental HE_{11}-mode. First the atoms are in a mixture

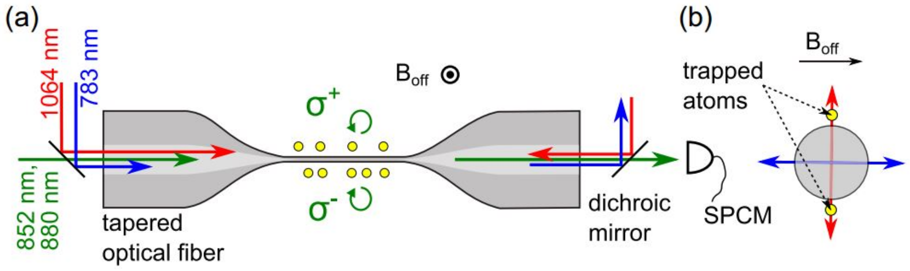

Figure 3.3: Fig. a) The experimental setup consists of the tapered optical fibre, the laser fields, and the single-photon counting module (SPCM). The green curved arrows show the circular polarization of the manipulation light fields.
Fig. b) Cross-section of the nano-fibre: The blue and red double arrows show the orientation of the linear polarizations of the blue- and red-detuned trapping fields. [39]

of the $F = 4$ hyperfine manifold. A magnetic field is applied to distinguish between the states and prevent spin flips. A manipulation light pulse is sent through the fibre. The light pulse is σ^+-polarized above the nano-fibre and σ^--polarized below it. The transmission spectrum of a subsequent probe pulse, that is resonant with the AC-Stark shifted $F = 4 \rightarrow F' = 5$ transition, is measured and confirms that the manipulation field pumped the atoms above the fibre toward $|F = 4, m_F = +4\rangle$ and the atoms below the fibre toward $|F = 4, m_F = -4\rangle$. With this method the particles on each side of the nano-fibre can be addressed independently.
In [25], this experimental setup is used to direct the spontaneous emission of photons by an atom into a specific propagation direction.

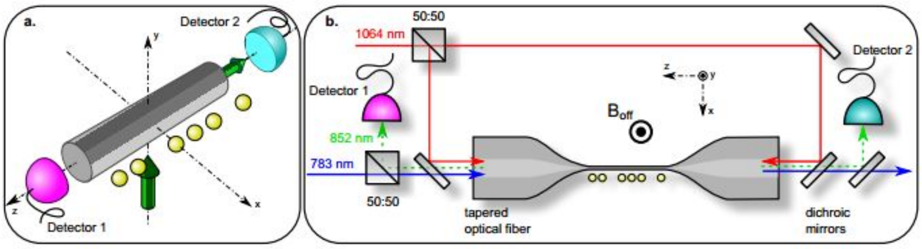

Figure 3.4: Experimental setup: Fig. a) shows atoms trapped on one side of the nano-fibre and excited by a σ^--polarized laser beam. A detector at the ends of the fibre detects the fluorescence light emitted by the atoms.
Fig. b) additionally shows the tapered optical fibre, the dipole trap lasers (blue and red lines), the resonant light beam paths (green dotted lines), and the atoms along the nano-fibre. B_{off} demonstrates the direction of the homogeneous offset magnetic fields. [25]

Fig. 3.4 shows the experimental setup, where spontaneous emission of light by quantum emitters into nano-fibres, using caesium atoms along a vacuum-clad silica nano-fibre, are

investigated. Here, only atoms on one side of the fibre are prepared. The polarization properties of the guided modes lead to directional spontaneous emission into the nanofibre. The scattering rate of an atom at position $\mathbf{r}$ is proportional to $|\mathbf{d}^* \cdot \mathbf{u}(\mathbf{r})|^2$, with the atomic dipole operator $\mathbf{d}$ and local unit polarization vector $\mathbf{u}$. As the local spin changes sign when reversing the propagation direction of the guided field, the coupling between the light's spin and orbital angular momentum allows to control the direction of spontaneous emission.
They prepared the atoms in the outermost Zeeman substate $|F = 4, m_F = -4\rangle$. A magnetic offset field is used to avoid spin flips and to distinguish between the states. By an external σ^--polarized laser field the atomic transition $|F = 4, m_F = -4\rangle \rightarrow |F' = 5, m_{F'} = -5\rangle$ is driven. For this transition the atoms only emit σ^--polarized light and most of the light is detected by one detector. [25]

3.4 Trapping of ultracold atoms in a hollow-core photonic crystal fibre

In hollow-core fibres, the atoms are directly positioned into a capillary in the centre of the fibre and thus coupled to the fibre mode. The problem here is, that this system can not directly be connected to the fibre network, because at least one end of the hollow-core fibre has to be positioned in the vacuum chamber [4].
The experimental setup of such a trap, can be seen in Fig. 3.5. To trap atoms in a hollow-core fibre, one uses a red detuned optical dipole trap positioned at the end of a hollow-core photonic crystal fibre, which is hold by a vacuum chamber. This fibre has to be large enough, so that atoms can enter. The atoms can move between these two traps, by changing the intensities of the two traps. The laser beam is focused onto the fibre tip from outside the vacuum chamber. At the other side of the fibre is a retractable mirror to detect the outgoing light. The laser is far detuned, so that radiation pressure,

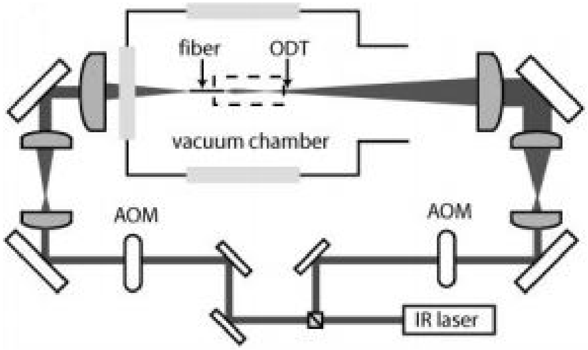

Figure 3.5: The beams used to trap are first order diffracted beams from acousto-optic modulators. [40]

heating and trap loss can be neglected. [40]

Chapter 4

Optical forces and dynamics for symmetric pumping $\alpha = \beta$

In this chapter we calculate the force for a set of particles with one transverse laser field and two incoming longitudinal fields. First we start with analytical results with only one particle, then we enlarge the system to two, three and four particles. Afterwards we concentrate on numerical results for larger systems. For all of these first results we assume symmetric scattering with $\alpha = \beta = 1/\sqrt{2}$ and thus $\theta = \pi/4$. In the next chapter we will concentrate on the case with asymmetric scattering, thus $\alpha \neq \beta$.

4.1 Optical forces on a single particle

For one beam-splitter, as we see in Fig. 4.1, we have the incoming longitudinal beams $B_1 = \sqrt{2I_l/(c\epsilon_0)}\exp(ik(x-x_0)+\phi_B)$ and $C_1 = \sqrt{2I_l/(c\epsilon_0)}\exp(-ik(x-x_0)+\phi_C)$, and the transverse pump $\eta = \sqrt{2I_\eta/(c\epsilon_0)}\exp(\phi_\eta)$. Defining $x_0 = (\phi_B - \phi_C)/(2k)$, there only remains the phase difference between longitudinal and transverse pump fields $\phi = (\phi_B+\phi_C)/2 - \phi_\eta$. First we calculate the intensities, using Eq. (2.31) and Eq. (2.32):

$$I_{ol} = \frac{c\epsilon_0}{2}|A_1|^2 = \frac{\left|\zeta\sqrt{I_l}e^{ikx} + i\sqrt{I_r}e^{-ikx} + (i+\zeta)\sqrt{\frac{I_\eta}{2}}e^{-i\phi}\right|^2}{1+|\zeta|^2}, \tag{4.1}$$

$$I_{or} = \frac{c\epsilon_0}{2}|D_1|^2 = \frac{\left|\zeta\sqrt{I_r}e^{-ikx} + i\sqrt{I_l}e^{ikx} + (i+\zeta)\sqrt{\frac{I_\eta}{2}}e^{-i\phi}\right|^2}{1+|\zeta|^2}. \tag{4.2}$$

For some examples of the outgoing intensities, see Fig. 4.2.
In the next step, we calculate the force on one beam-splitter. We use Eq. (2.52) and

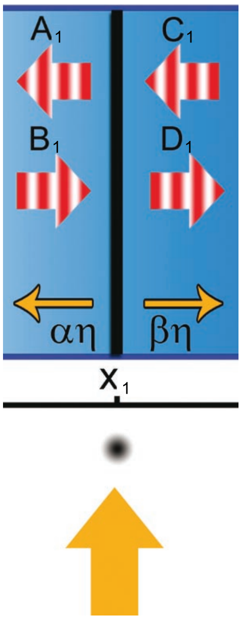

Figure 4.1: One beam-splitter with incoming longitudinal fields B_1 and C_1, transverse pump η, and outgoing fields A_1 and D_1.

obtain:

$$\begin{aligned} F_1 =& \frac{\epsilon_0}{2}\left(|A_1|^2 + |B_1|^2 - |C_1|^2 - |D_1|^2\right) \\ =& \frac{(I_l - I_r)\left(|\zeta|^2 + \zeta_i\right) - 2\sqrt{I_l I_r}\zeta_r \sin(2kx)}{\frac{c}{2}|1 - i\zeta|^2} \\ &+ \frac{\sqrt{2I_\eta}}{c}\left(\sqrt{I_r}\cos(kx - \phi) - \sqrt{I_l}\cos(kx + \phi)\right). \end{aligned} \tag{4.3}$$

The second line of Eq. (4.3) represents the force, emerging from the counter-propagating fields in the fibre as in Eq. (2.53). The last line arises from interference between the longitudinal fields and the transverse pump. Our matter of concern is to find the stable configurations of our system, which means on one side, that the force is zero, and on the other side that the derivative of the force with respect to the position of the beam-splitter is negative. Different cases for various parameters are shown in Fig. 4.3. It is interesting that introducing the transverse pump η changes the periodicity from $\lambda/2$ to λ.

As seen in Fig. 4.3b), for special ζ and large difference between I_l and I_r, there do not exist zero-points any more. We want to examine this behaviour in more detail, after calculating the potential of such a system.

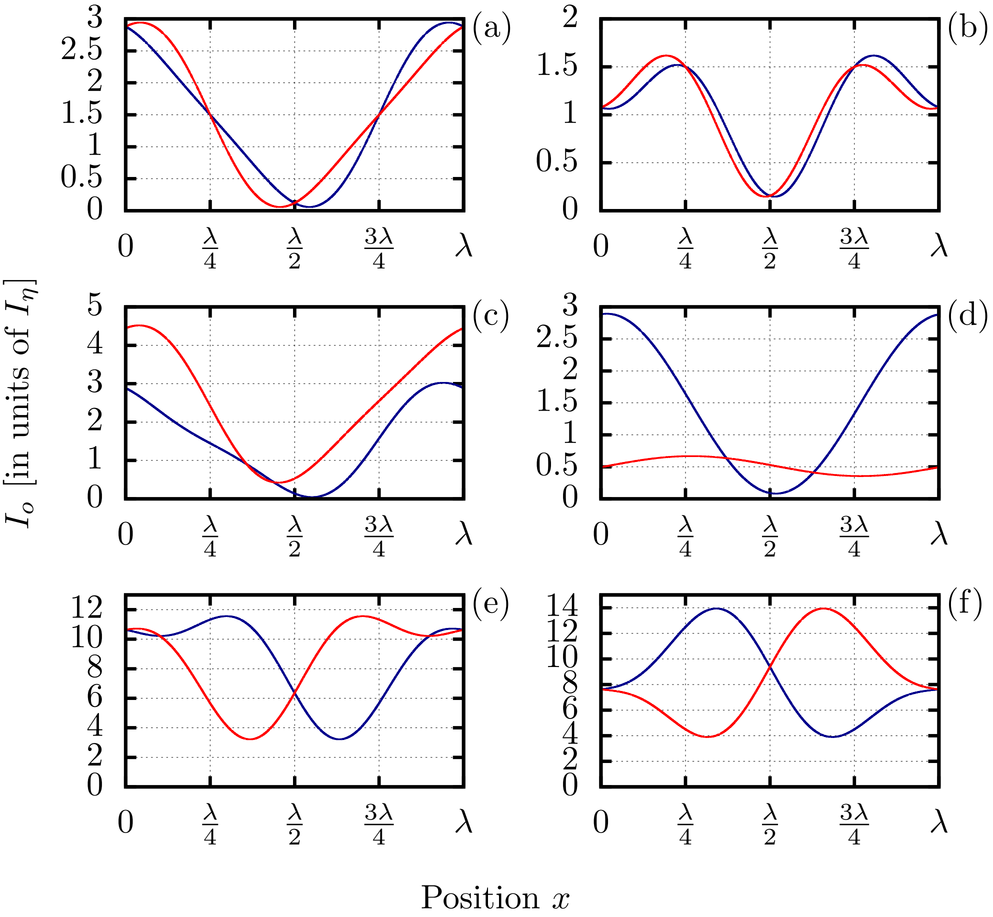

Figure 4.2: Intensities I_{ol} (blue) and I_{or} (red) for
a) $I_l = I_r = I_\eta$, $\phi = 0$ and $\zeta = 1/9$,
b) $I_l = I_r = I_\eta$, $\phi = 0$ and $\zeta = 1/9 + i/2$,
c) $I_l = 2I_\eta$, $I_r = I_\eta$, $\phi = 0$ and $\zeta = 1/9$,
d) $I_l = 0$, $I_r = I_\eta$, $\phi = 0$ and $\zeta = 1/9$,
e) $I_l = I_r = 8I_\eta$, $\phi = \pi/4$ and $\zeta = 1/9$, and
f) $I_l = I_r = 8I_\eta$, $\phi = \pi/2$ and $\zeta = 1/9$.
For $I_l = I_r = I_\eta$, we have $I_{ol}(x) = I_{or}(\lambda - x)$. The imaginary part of ζ reduces the outgoing intensity, because of absorption. Looking at Fig. c) and d), we can see that for different incoming intensities and small ζ, which means that most of the light is transmitted, the outgoing intensity is mostly larger at the opposite side of the higher incoming intensity. Fig. e) and f) show the outgoing intensities for $\phi \neq 0$, which rather changes the intensities.

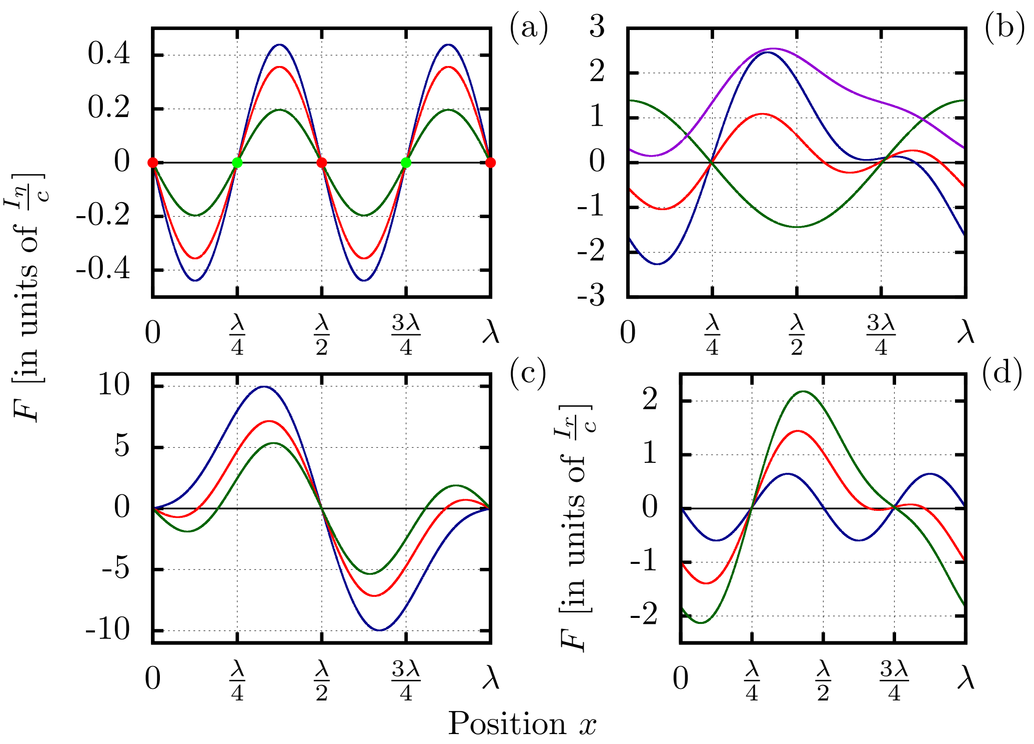

Figure 4.3: Forces F on one beam-splitter for
a) $I_l = I_r = I_\eta$, $\phi = 0$, $\zeta = 1/9$ (blue), $\zeta = 1/9 + i/9$ (red) and $\zeta = 1/9 + i/2$ (green),
b) $\phi = 0$, $I_r = I_\eta$, $I_l = 5I_\eta$, $\zeta = 1/9$ (blue), $I_l = 2I_\eta$, $\zeta = 1/9$ (red), $I_l = 0$, $\zeta = 1/9$ (green), $I_l = 3I_\eta$ and $\zeta = 1/9 + i/2$ (violet).
c) $I_l = I_r = 8I_\eta$, $\zeta = 1/9$, $\phi = \pi/2$ (blue), $\phi = \pi/3$ (red) and $\phi = \pi/4$ (green),
d) $I_l = 2I_\eta$, $\phi = 0$, $\zeta = 1/9$, $I_\eta = 0$ (blue), $I_\eta = 3I_r$ (red) and $I_\eta = 10I_r$ (green).
Red points correspond to stable points, while green points are unstable.
Fig. a) is the same case as $I_\eta = 0$. We see that this case is $\lambda/2$-periodic and we have four zero-points per wavelength, two of them are stable (green points). Because of absorption, an imaginary part of ζ reduces the absolute value of the force.
Fig. b) shows the force for $I_r = I_\eta$ and different I_l, which changes the number of zero-points. For large difference between I_l and I_r, we have only two zero-points per wavelength, while we have four zero-points for smaller differences. An imaginary part of ζ pushes the force toward the weaker source. For a large imaginary part of ζ and a large difference between I_l and I_r, there are no zero-points any more (green line).
Changing ϕ can also influence the number of zero-points. Looking at Fig. c), we see that the zero-point at $x = 0$ or $x = \lambda$ is not stable for the blue line, but gets stable, when new zero-points appear, as for the red and green line.
This phenomenon inversely appears for different I_η (Fig. d)). For a larger I_η, we have only two zero-points per wavelength, but the zero-point at $x = 3\lambda/4$ is stable.
It is also interesting that I_η changes the periodicity to λ.

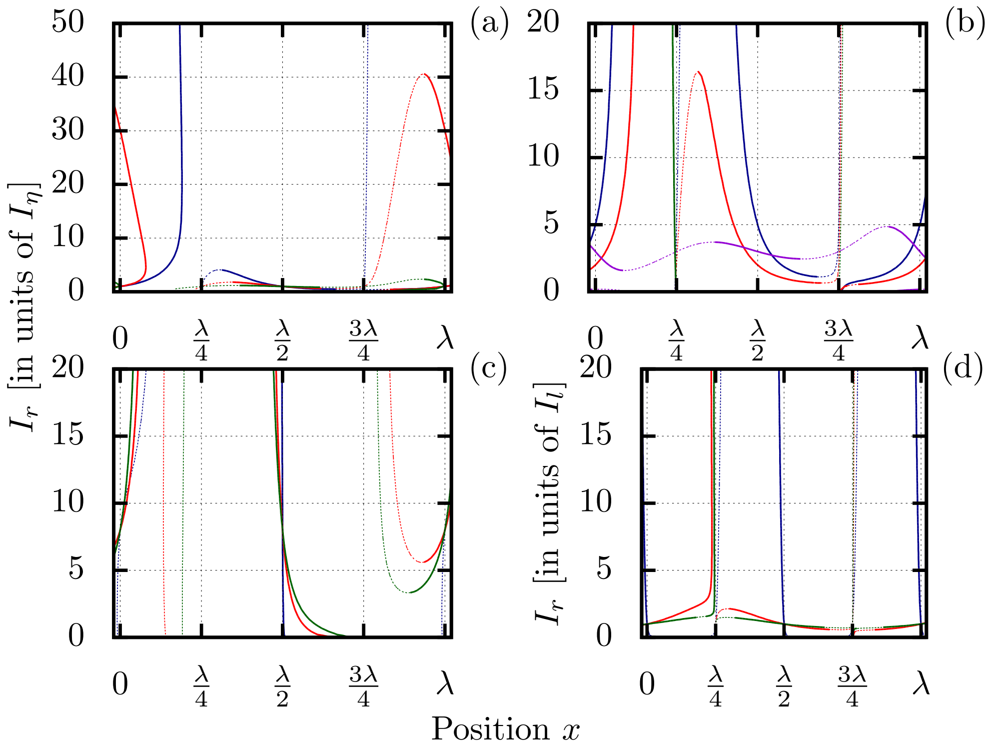

Figure 4.4: zero-points of the force on a single beam-splitter for
a) $I_l = I_\eta$, $\phi = 0$, $\zeta = 1/9$ (blue), $\zeta = 1/9 + i/9$ (red) and $\zeta = 1/9 + i/2$ (green),
b) $\phi = 0$, $I_l = 5I_\eta$, $\zeta = 1/9$ (blue), $I_l = 2I_\eta$ and $\zeta = 1/9$ (red), $I_l = 0$, $\zeta = 1/9$ (green), $I_l = 3I_\eta$ and $\zeta = 1/9 + i/2$ (violet).
c) $I_l = 8I_\eta$, $\zeta = 1/9$, $\phi = \pi/2$ (blue), $\phi = \pi/3$ (red) and $\phi = \pi/4$ (green),
d) $\phi = 0$, $\zeta = 1/9$, $I_\eta = 0$ (blue), $I_\eta = 3I_l$ (red) and $I_\eta = 10I_l$ (green).
Solid lines correspond to stable points.
Fig. a) shows that we can get more zero-points for small difference between I_r and I_l and real ζ (red). For large ζ_i and large difference between the intensities of the counter-propagating fields, we can not even get one zero-point (blue and green). This phenomenon is also confirmed in Fig. b). Changing ϕ also leads to interesting effects. For special ϕ exists a threshold above which four zero-points can be found (Fig. c)). For different I_η we can obtain four zero-points at $I_l \approx I_r$.

4.1.1 Potential for a single beam-splitter

For a single beam-splitter we can easily calculate a potential by integrating the force:

$$V(x) = -\int_0^x F(x\prime)dx\prime. \tag{4.4}$$

Here we are lucky that the radiative pressure force proportional to ζ_i is just a constant, not preventing to obtain a potential. The potential helps to understand, whether a zero force point is stable or not. For a detailed discussion see [6].
Inserting Eq. (4.3) into Eq. (4.4), we obtain:

$$\begin{aligned} V(x) =& \frac{2(I_r - I_l)\left(|\zeta|^2 + \zeta_i\right)kx + 2\sqrt{I_l I_r}\zeta_r\left(1 - \cos(2kx)\right)}{kc|1 - i\zeta|^2} \\ &+ \frac{\sqrt{2I_\eta}}{kc}\left(\sqrt{I_l}(\sin(kx + \phi) - \sin(\phi)) - \sqrt{I_r}(\sin(kx - \phi) + \sin(\phi))\right). \end{aligned} \tag{4.5}$$

In Fig. 4.5 we can see some examples for different parameters of the potential. As a potential minimum corresponds to a stable point, we can find a condition for the points to be stable. A minimum of the potential means that the derivative of the force in this point is negative.

4.1.2 Large asymmetries of I_l and I_r

Examining Eq. (4.3), we can already see that for large difference between I_l and I_r no x that fulfils the condition $F(x) = 0$ exists, thus we can not find any zero-point and the particle is unstable. To investigate this behaviour, we set $F(x) = 0$ and rewrite the equation:

$$\begin{aligned} I_l =& (\frac{1}{16(\zeta_i + |\zeta|^2)^2}\left(\sqrt{2I_\eta}\cos(\phi + kx)|1 - i\zeta|^2 + 4\sqrt{I_r}\zeta_r\sin(2kx) + \sqrt{-8\sqrt{Ir}(\zeta_i + |\zeta|^2)(\sqrt{2I_\eta}\cos(\phi - kx)|1 - i\zeta|^2 - 2\sqrt{Ir}(\zeta_i + |\zeta|^2)) + (\sqrt{2I_\eta}\cos(\phi + kx)|1 - i\zeta|^2 + 4\sqrt{I_r}\zeta_r\sin(2kx))^2}\right)^2 \\ <& \frac{1}{16(\zeta_i + |\zeta|^2)^2}\left(\sqrt{2I_\eta}|1 - i\zeta|^2 + 4\sqrt{I_r}\zeta_r + \sqrt{8\sqrt{Ir}(\zeta_i + |\zeta|^2)(\sqrt{2I_\eta}|1 - i\zeta|^2 + 2\sqrt{Ir}(\zeta_i + |\zeta|^2)) + (\sqrt{2I_\eta}|1 - i\zeta|^2 + 4\sqrt{I_r}\zeta_r)^2}\right)^2. \end{aligned} \tag{4.6}$$

Eq. (4.6) shows that there must exist a maximum of I_l for every I_r, so that no zero-point can be found after exceeding this threshold.

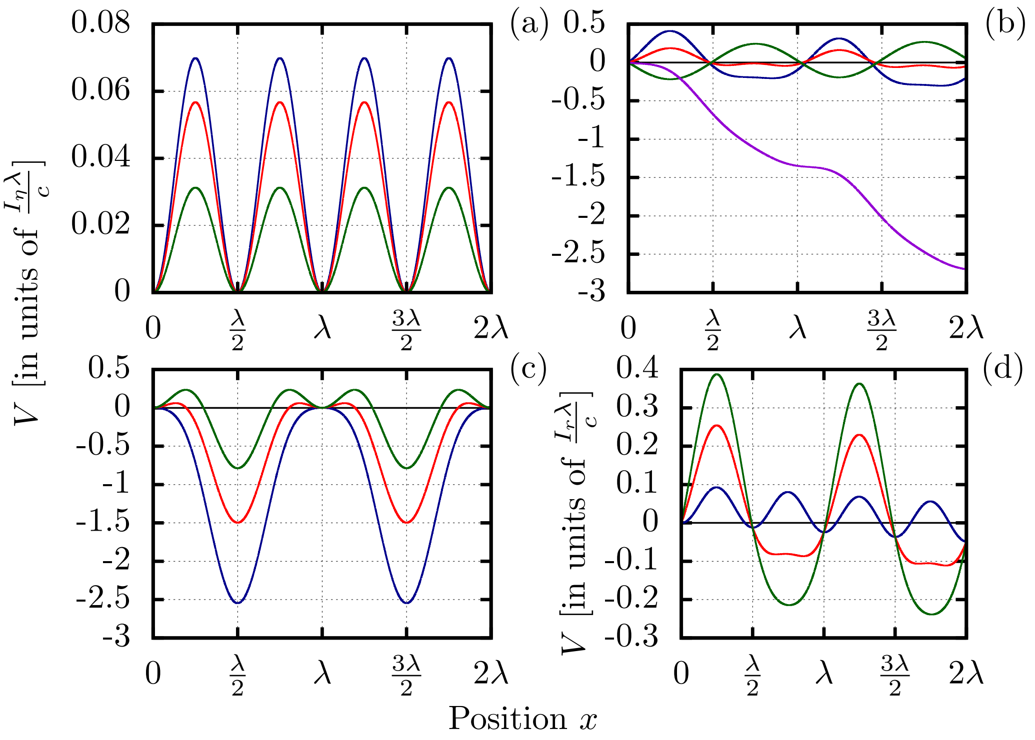

Figure 4.5: Potential for a single beam-splitter as function of the position of the beam-splitter x for
a) $I_l = I_r = I_\eta$, $\phi = 0$ and $\zeta = 1/9$ (blue), $\zeta = 1/9 + i/9$ (red) and $\zeta = 1/9 + i/2$ (green),
b) $\phi = 0$, $I_r = I_\eta$ and $I_l = 5I_\eta$ and $\zeta = 1/9$ (blue), $I_l = 2I_\eta$ and $\zeta = 1/9$ (red), $I_l = 0$ and $\zeta = 1/9$ (green), and $I_l = 3I_\eta$ and $\zeta = 1/9 + i/2$ (violet).
c) $I_l = I_r = 8I_\eta$, $\zeta = 1/9$ and $\phi = \pi/2$ (blue), $\phi = \pi/3$ (red) and $\phi = \pi/4$ (green),
d) $I_l = 2I_\eta$, $\phi = 0$, $\zeta = 1/9$ and $I_\eta = 0$ (blue), $I_\eta = 3I_r$ (red) and $I_\eta = 10I_r$ (green).
Potential minima corresponds to stable points.
This figure again confirms the results of Fig. 4.3.
We see that for asymmetric longitudinal beams $I_l \neq I_r$ the potential is increasing or decreasing as shown in Fig. c) and d). While $I_l = I_r = I_\eta$ and $\phi = 0$ produce four stable positions per wavelength in Fig. a), we do not even get one stable point for large asymmetry between I_l and I_r and including absorption (Fig. b) violet line). By changing ϕ, we can obtain additional stable points as shown in Fig. c). Fig. d) demonstrates how an unstable point can get stable by changing I_η.

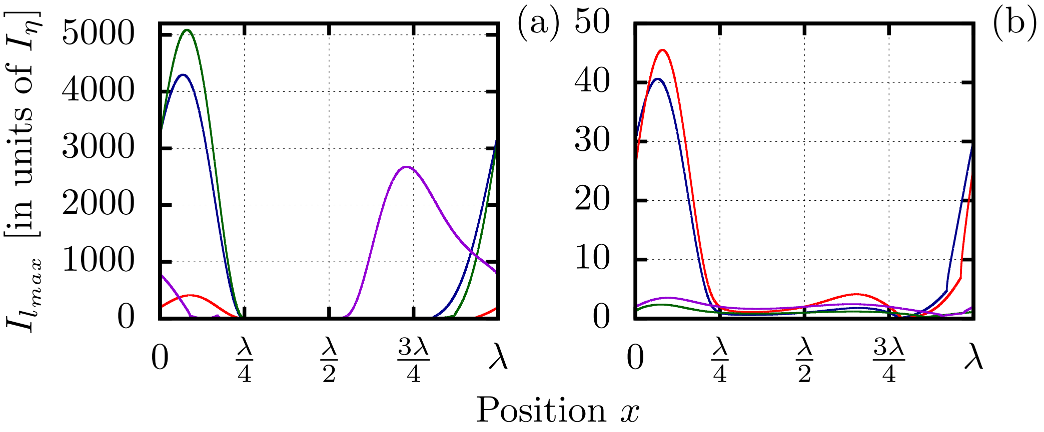

Figure 4.6: Maximum left incoming intensity $I_{l_{max}}$ on one beam-splitter for
a) $I_r = I_\eta$, $\phi = 0$ and $\zeta = 1/9$ (blue), $I_r = I_\eta$, $\phi = 0$ and $\zeta = 2/9$ (red), $I_r = 2I_\eta$, $\phi = 0$ and $\zeta = 1/9$ (green), and $I_r = I_\eta$, $\phi = \pi/3$ and $\zeta = 1/9$ (violet).
b) $I_r = I_\eta$, $\phi = 0$ and $\zeta = 1/9 + j/9$ (blue), $I_r = 2I_\eta$, $\phi = 0$ and $\zeta = 1/9 + j/9$ (red), $I_r = I_\eta$, $\phi = 0$ and $\zeta = 1/9 + j/2$ (green), and $I_r = 2I_\eta$, $\phi = 0$ and $\zeta = 1/9 + j/2$ (violet). Even a small imaginary part of ζ decreases $I_{l_{max}}$ by several orders of magnitude and destabilizes the system. The same effect is shown for ζ_r, which pushes the system toward an intensity maximum or minimum. It is intuitive that a larger I_r increases the maximum of I_l.

Fig. 4.6 demonstrates some examples for the maximum of I_l, below which we can find zero-points of the force 4.3. It is intuitively clear that a larger I_r increases the maximum of I_l. The force stemming from the imaginary part of ζ pushes the particles toward the weaker source. The strength of this push is proportional to the difference of the incoming intensities as we can see in Eq. (4.3). So a larger ζ_i encourages the influences on the force of the difference between I_l and I_r.
The same counts for the real part of ζ. ζ_r increases the force toward the intensity maximum or minimum, which forces instabilities as shown in Fig. 4.7a). Such a maximum for ζ and the asymmetry of the incoming light are also found for only counter-propagating light [6]. For the imaginary part of ζ this effect already appears for small values, if we have high asymmetries between I_l and I_r (Fig. 4.7b)). It is also interesting that ζ affects the height of this maximum more than I_r. As long as enough light is transmitted, meaning ζ small, the imbalance in the incoming amplitudes can be counteracted by the outgoing imbalance. For some special ζ_r new zero-points can appear as for the green line in Fig. 4.7a).

4.1.3 Special cases

To simplify and examine the system with one beam-splitter in more detail, we concentrate on some special cases, which allow us to find stable configurations analytically.

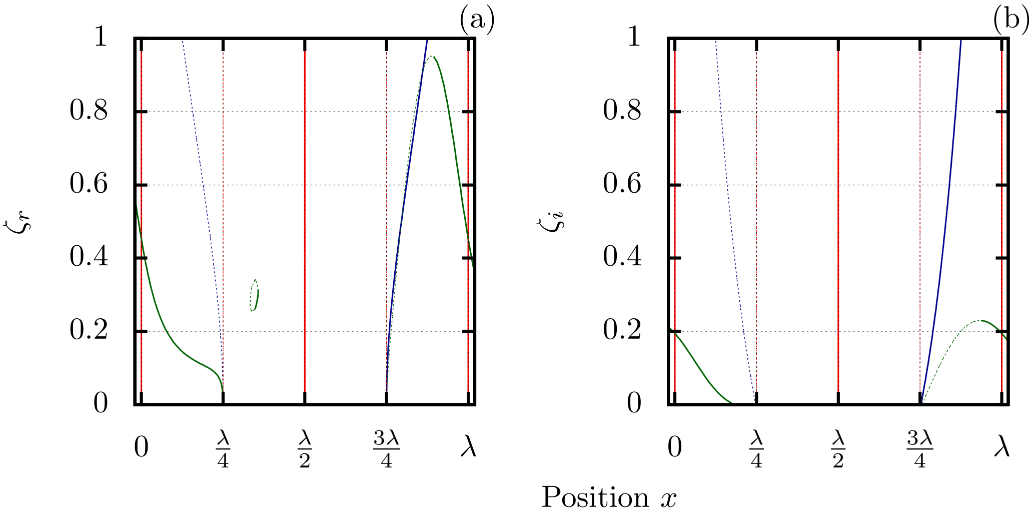

Figure 4.7: zero-points of the force on a single beam-splitter as function of the position of the beam-splitter x and $\Re(\zeta)$ (Fig. a)) or $\Im(\zeta)$ (Fig. b)) for $I_l = I_\eta$ and $\phi = 0$. The blue line corresponds to $I_r = 0$, the red line to $I_r = I_\eta$ and the green line to $I_r = 10I_\eta$. The solid lines show the stable zero-points, while the dashed lines show the unstable ones. Fig. a) Looking at the green line, we find for a small region of ζ additional zero-points. Fig. b) We set $\Re(\zeta) = 1/9$.

For large asymmetries between left and right counter-propagating incoming light and large ζ_r, we can not find any stable positions as we have already seen in Fig. 4.6. For ζ_i this effect already appears for small values.

Stability for small $\zeta \ll 1$

As in general ζ is small and most of the light is transmitted through the particles, we will study this case separately in more details. We choose $\zeta \in \Re$, and drop terms of $\mathcal{O}(\zeta^2)$ and higher. With these assumptions, the force is given by:

$$F = \frac{\sqrt{2I_\eta}}{c}\left(\sqrt{I_r}\cos(kx-\phi) - \sqrt{I_l}\cos(kx+\phi)\right) - \frac{4\zeta\sqrt{I_l I_r}}{c}\sin(2kx). \tag{4.7}$$

Assuming „in phase“ transverse pump $\phi = 0$, Eq. (4.7) changes to:

$$F = \sqrt{2I_\eta}(\sqrt{I_r} - \sqrt{I_l})\cos(kx) - 4\zeta\sqrt{I_l I_r}\sin(2kx), \tag{4.8}$$

and we can easily find the stable points of this equation:

$$kx = \begin{cases} \arcsin\left(\frac{\sqrt{2I_\eta}(\sqrt{I_r}-\sqrt{I_l})}{8\zeta\sqrt{I_l I_r}}\right) + 2\pi n & \text{if } I_l, I_r \neq 0, \zeta > 0, \\ \pi - \arcsin\left(\frac{\sqrt{2I_\eta}(\sqrt{I_r}-\sqrt{I_l})}{8\zeta\sqrt{I_l I_r}}\right) + 2\pi n & \text{if } I_l, I_r \neq 0, \zeta > 0, \\ \frac{4n+1}{2}\pi & \text{if } \zeta < \sqrt{\frac{2I_\eta}{I_l I_r}}\frac{(\sqrt{I_r}-\sqrt{I_l})}{8} \text{ or } I_l, I_r = 0, \\ \frac{4n+3}{2}\pi & \text{if } \zeta > \sqrt{\frac{2I_\eta}{I_l I_r}}\frac{(\sqrt{I_r}-\sqrt{I_l})}{8} \text{ or } I_l, I_r = 0, \end{cases} \tag{4.9}$$

with $n \in \mathbb{N}$. Obviously, the first two zero-points only exist for $|\sqrt{2I_\eta}(\sqrt{I_r}-\sqrt{I_l})/(8\zeta\sqrt{I_l I_r})| < 1$.

It is interesting to see that, in contrast to Eq. (4.6), the difference between I_l and I_r is not limited for this case and we are able to find zero-points of the force for every I_l-I_r combination. As we have already seen in Eq. (4.6) and Fig. 4.6, for small values of ζ, we have a larger threshold. As for $\zeta \to 0$ all the light is transmitted through the particles, the outgoing intensities can compensate the incoming ones and this threshold vanishes.

Fig. 4.8 compare the exactly solved Eq. (4.3) and the approximate force Eq. (4.7).

Stability of the particles in a standing wave $I_l = I_r$ and additional transverse pump

If we choose small intensity differences of the dipole force, the first term of Eq. (4.3) can be neglected and the force for $I_l = I_r = I$ reads:

$$F = \frac{2\sin(kx)}{c}\left(\frac{-4I\zeta_r\cos(kx)}{|1-i\zeta|^2} + \sqrt{2I_\eta I}\sin(\phi)\right). \tag{4.10}$$

Eq. (4.10) clearly separates longitudinal beams I and transverse pump I_η. Without transverse pump $I_\eta = 0$ we get a simple standing wave with period $\lambda/2$. We have

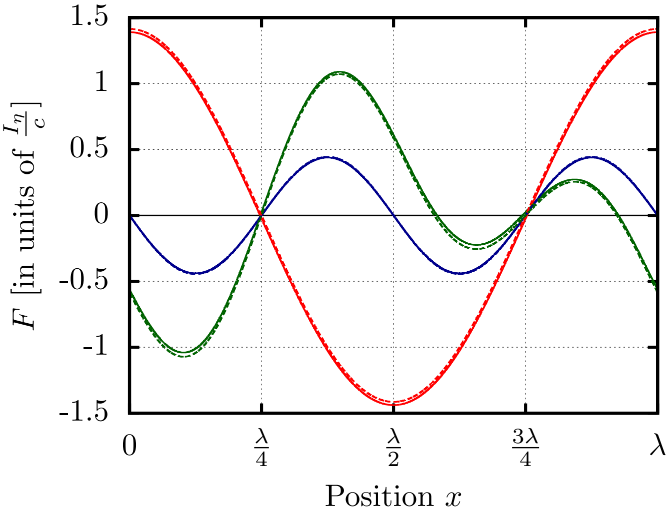

Figure 4.8: Comparison between the exactly solved force Eq. (4.3) (solid lines) and the approximated force Eq. (4.7) (dashed lines) for small $\zeta = 1/9$. The blue line corresponds to $I_l = I_r = I_\eta$, the red line to $I_l = 0$ and $I_r = I_\eta$ and the green line to $I_l = 2I_\eta$ and $I_r = I_\eta$. The approximate force does not differ much from the exactly solved one.

the same phenomenon for real transverse pump, meaning $\phi = 0$. Switching on the transverse pump or changing to $I_l \neq I_r$ modify this periodicity to λ. For this system the zero-points of Eq. (4.10) can easily be found. The following are the stable ones, which means $\partial F/\partial x < 0$:

$$kx = \begin{cases} 2n\pi, & \text{if } \sin(\phi) < \frac{2\sqrt{2I}\zeta_r}{\sqrt{I_\eta}|1-i\zeta|^2}, \\ (2n+1)\pi, & \text{if } \sin(\phi) > \frac{-2\sqrt{2I}\zeta_r}{\sqrt{I_\eta}|1-i\zeta|^2}, \\ \pm\arccos\left(\sqrt{\frac{I_\eta}{2I}}\frac{|1-i\zeta|^2}{2\zeta_r}\sin(\phi)\right) + 2n\pi, & \text{if } \zeta_r < 0, \end{cases} \tag{4.11}$$

The stable positions in the last line only exist for $|\sin(\phi)| \leq 2\sqrt{2I}\zeta_r/(\sqrt{I_\eta}|1-i\zeta|^2)$. Fig. 4.9 shows some typical examples for the force and its stable points. Choosing $\zeta_r > 0$ the first stationary position at $x = 0$ (or $x = \lambda$) is only stable as long as extra unstable zeros at $kx = \pm\arccos\left(\sqrt{I_\eta/(2I)}\frac{|1-i\zeta|^2}{2\zeta_r}\sin(\phi)\right) + 2n\pi$ (Eq. 4.11, condition 3) exist.

Stability of the outermost particle

In this section we examine the case of one particle with a longitudinal beam only impinging from the left. This particle corresponds to the outermost particle of a multiparticle configuration with only transverse pump. For this example the incoming light on the particles arises through reflection and transmission of the transverse pump by all the other particles in the system. This case is important, in the sense that in a

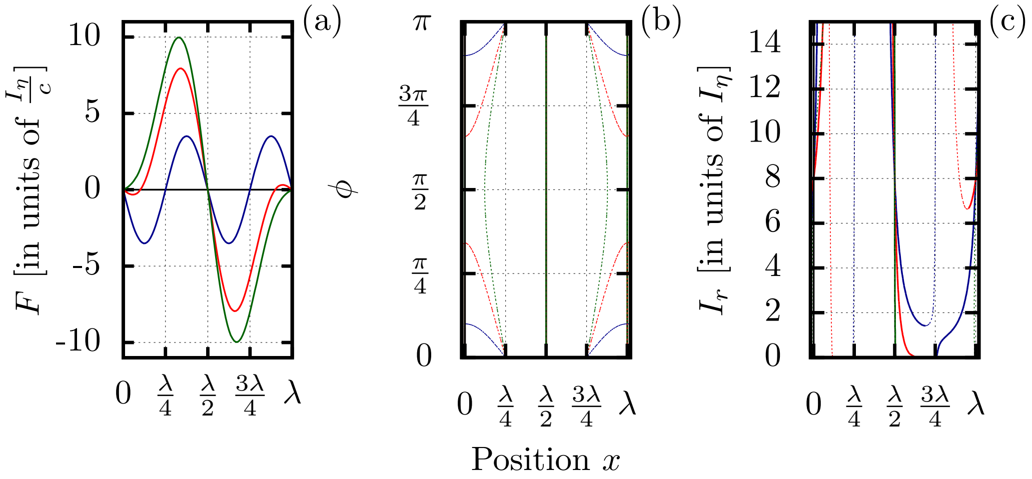

Figure 4.9: Fig. a) shows the force on a single beam-splitter for $I_l = I_r = 8I_\eta$ and $\zeta = 1/9$. The blue line corresponds to $\phi = 0$, the red line to $\phi = \pi/4$ and the green line to $\phi = \pi/2$. We see that the particle trap positions at integer multiples of λ get unstable for $\phi = \pi/2$, cf. equation (4.11).
Fig. b) shows the zero-points of the force on one beam-splitter as function of the position of the beam-splitter x and ϕ for $\zeta = 1/9$ and $I_l = I_r = I$. The blue line corresponds to $I = I_\eta$, the red line to $I = 8I_\eta$ and the green line to $I = 20I_\eta$.
In Fig. c) we plot the dependence of the zero force position x for varying pump right field power I_r for $\zeta = 1/9$ and $I_l = 8I_\eta$. The blue line corresponds to $\phi = 0$, the red line to $\phi = \pi/4$ and the green line to $\phi = \pi/2$.
For Fig. b) and c), the solid lines show the stable zero-points, while the dashed lines show the unstable ones.
Comparing Fig. c) with Fig. a) we see that the figures correspond to each other at $I_r = 8I_\eta$. It is interesting that for some ϕ's new zero-points appear after exceeding a special threshold.

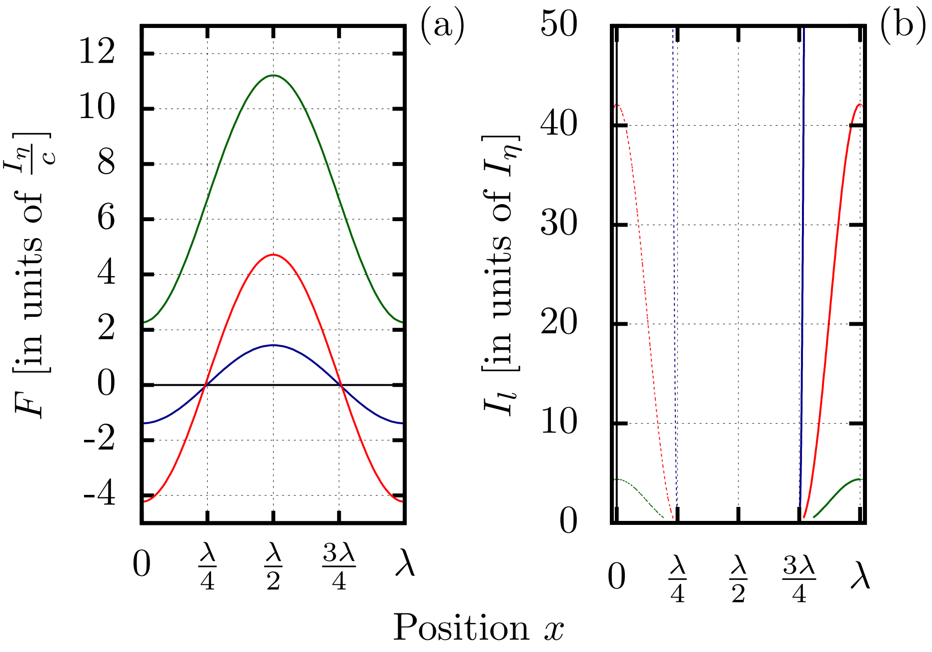

Figure 4.10: Fig. a) shows the force on a single beam-splitter for $I_r = 0$ and $\phi = 0$. The blue line corresponds to $I_l = I_\eta$ and $\zeta = 1/9$, the red line to $I_l = 10 I_\eta$ and $\zeta = 1/9$ and the green line to $I_l = 10 I_\eta$ and $\zeta = 1/9 + i/2$.
Fig. b) demonstrates the zero-points of the force on one beam-splitter as function of the position of the beam-splitter x and I_l for $\phi = 0$ and $I_r = 0$. The blue line corresponds to $\zeta = 1/9$, the red line to $\zeta = 1/9 + i/9$ and the green line to $\zeta = 1/9 + i/2$. The solid lines show the stable zero-points, while the dashed lines show the unstable ones.
As we can already see in Eq. (4.14) for I_l exists a limit, where the system gets unstable. For imaginary ζ this limit is lower as shown in Fig. b). The green line in Fig. a) shows an example for a system without stable points.

system of many particles, the configuration can only be stable, if at least the outermost particle is stable. Inserting $I_r = 0$ into Eq. (4.3) we get:

$$F = \frac{1}{c}\left(\frac{2I_l\left(|\zeta|^2 + \zeta_i\right)}{|1 - i\zeta|^2} - \sqrt{2I_\eta I_l}\cos(kx + \phi)\right). \tag{4.12}$$

For this case the stable zero-points read:

$$kx = -\arccos\left(\frac{\sqrt{2}(\zeta_i + |\zeta|^2)\sqrt{I_l}}{|1 - i\zeta|^2\sqrt{I_\eta}}\right) - \phi + 2n\pi, n \in \mathbb{N}. \tag{4.13}$$

These zero-points only exist for:

$$\frac{I_\eta}{I_l} \geq \left(\frac{\sqrt{2}(\zeta_i + |\zeta|^2)}{|1 - i\zeta|^2}\right)^2, \tag{4.14}$$

hence, I_η/I_l has to exceed a special threshold. As I_l is proportional to I_η, this means that I_l has an upper threshold that limits the possibility to find stable points as we have already seen earlier for $I_l \neq I_r \neq 0$. The threshold of I_l is also limited by ζ_i. This is also confirmed by Fig. 4.10, where we plotted some examples for the force and its zero-points.

4.2 Multiparticle systems

In this section we examine configurations with more than one particle. Here, the motion is split into centre of mass and relative motion. So we can find configurations, where the particles move together, but keep a fixed distance. To get fully stable configurations we also need the condition of a vanishing centre of mass motion, which can be obtained from the outermost field amplitudes:

$$F_{tot} = \frac{\epsilon_0}{2}(|A_1|^2 + |B_1|^2 - |C_N|^2 - |D_N|^2) = 0, \tag{4.15}$$

with particle number N.

Although the equation of the force Eq. (2.52) looks quite easy, the squares of the absolute values generate very large expressions for larger systems. So we only take a short look at systems with $I_l, I_r \neq 0$ and then in general set $I_l = I_r = 0$.

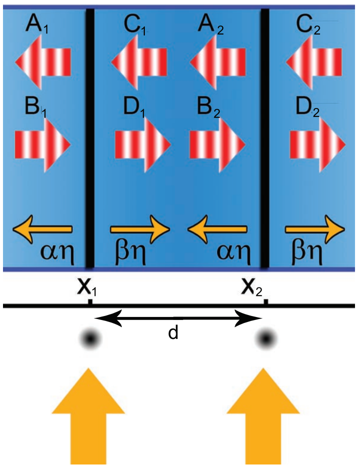

Figure 4.11: A system with two particles at distance d, counter-propagating incoming fields B_1 and C_2, transverse pump η and outgoing fields A_1 and D_2.

4.2.1 Optical forces on two particles

Fig. 4.11 shows the system for two particles. As shown in Eq. (2.39), we can calculate the amplitudes as follows:

$$\begin{pmatrix} A_1 \\ B_1 \\ \eta \end{pmatrix} = M_{BS} \cdot P(d) \cdot M_{BS} \begin{pmatrix} C_2 \\ D_2 \\ \eta \end{pmatrix}, \tag{4.16}$$

with M_{BS} being the beam-splitter matrix Eq. (2.36) and $P(d)$ the propagation matrix from Eq. (2.38).

So we can easily calculate the outgoing intensities, which are connected to the amplitudes A_1 and D_2 via $A_1 = \sqrt{2I_{ol}/(c\epsilon_0)}\exp(ikx_1)$ and $D_2 = \sqrt{2I_{or}/(c\epsilon_0)}\exp(i(k(x_1+d)))$, with x_1 the position of the first beam-splitter. Some examples of the intensities for $I_l, I_r \neq 0$, are shown in Fig. 4.12a).

Next we calculate the force F_1 on the first and F_2 on the second particle, using the following formula:

$$F_1 = \frac{\epsilon_0}{2}(|A_1|^2 + |B_1|^2 - |C_1|^2 - |D_1|^2), \tag{4.17}$$

$$F_2 = \frac{\epsilon_0}{2}(|A_2|^2 + |B_2|^2 - |C_2|^2 - |D_2|^2). \tag{4.18}$$

Choosing ζ small and neglecting terms of $O(\zeta^2)$ or higher, we obtain:

$$\begin{aligned} F_1 = &- 4\zeta\sqrt{I_l I_r}\sin(2kx_1) + I_\eta\left(\cos(kd) - \zeta\sin(2kd)\right) + \sqrt{2}\sqrt{I_\eta}\,\Big(\sqrt{I_r}\left(\cos(kx_1) + \zeta\sin(kx_1)\right) \\ &+ \sqrt{I_l}\left(\zeta\left(2\sin\left(k(d - x_1)\right) - \sin\left(k(2d + x_1)\right)\right) - \cos(kx_1)\right)\Big)\,, \end{aligned} \tag{4.19}$$

$$\begin{aligned} F_2 = &- 4\zeta\sqrt{I_l I_r}\sin(2k(d + x_1)) + I_\eta(\zeta\sin(2kd) - \cos(kd)) + \sqrt{2}\sqrt{I_\eta}\,\Big(\sqrt{I_l}\left(\zeta\sin(k(d + x_1))\right. \\ &\left. - \cos(k(d + x_1))\right) + \sqrt{I_r}\left(\zeta\left(\sin(k(d - x_1)) - 2\sin(k(2d + x_1))\right) + \cos(k(d + x_1))\right)\Big)\,, \end{aligned} \tag{4.20}$$

with x_1 the position of the left beam-splitter and real amplitudes B_1, C_2 and η. Here the first terms stem from the prescribed lattice ($\propto \sqrt{I_r I_l}$).

Some examples of the force on two beam-splitters are shown in Fig. 4.12b). We have chosen the position of the first particle x_1 so, that $F_1 = 0$ and $F_2 = 0$ at the stable equilibrium position. For two particles, configurations are stable, if the derivative of the force with respect to distance on the first beam-splitter is positive and negative on the right beam-splitter.

Because of the back-action of the particles on the light, larger systems are not conservative and we can not find a potential for them.

When we assume no incoming fields I_l, I_r it is possible to calculate the stable points and to see the influence of η. With this assumption the light scattered into the fibre by one particle only interferes with the scattered light of the second particle. This leads to strongly distance depending forces, where particles with low distance attract each other and start to repel at about half wavelength distance.

Calculating the intensities for this case, we get

$$I_{ol} = I_{or} = 2I_\eta\left|\frac{(1 - i\zeta)\cos(\frac{kd}{2})}{(1 - 2i\zeta)\cos(\frac{kd}{2}) - i\sin(\frac{kd}{2})}\right|^2, \tag{4.21}$$

with $I_{ol} = c\epsilon_0|A_1|^2/2$ and $I_{or} = c\epsilon_0|D_2|^2/2$. As we can see in Fig. 4.13a), because of symmetry, $I_{ol} = I_{or}$.

For the forces, this symmetry implies $F_1 = -F_2$, so that the centre of mass is force free. The force on the first particle reads:

$$F_1 = \frac{I_\eta|1 - i\zeta|^2\cos(kd)}{c\left(4\left(|\zeta|^2 + \zeta_i\right)\cos^2(\frac{kd}{2}) + 2\zeta_r\sin(kd) + 1\right)}. \tag{4.22}$$

Obviously the stable points are at:

$$d = \left(\frac{3}{4} + n\right)\lambda, \tag{4.23}$$

for $n \in \mathbb{N}$. It is really surprising that the stable distances for this case do not depend on ζ, not even on the imaginary part of ζ, which in general causes instabilities. Fig. 4.13b)

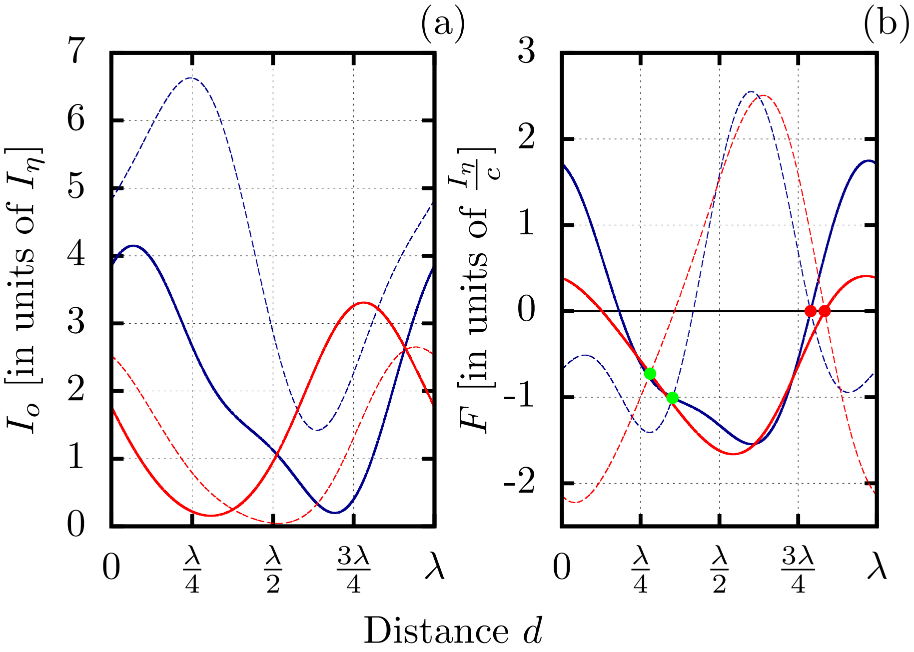

Figure 4.12: Fig. a) shows the outgoing intensities I_{ol} (solid line) and I_{or} (dashed line) as function of distance d for $\phi = 0$ and $\zeta = 1/9$.
Fig. b) shows the forces on two beam-splitters as function of distance d for $\phi = 0$ and $\zeta = 1/9$. The solid line shows the force on the first beam-splitter and the dashed line the force on the second one. The red points are stable equilibria and the green ones not. The blue lines correspond to $I_l = 3I_\eta$ and $I_r = I_\eta$, the red lines to $I_l = 0$ and $I_r = I_\eta$. Here the parameters are chosen to get zero centre of mass force at the stationary distance.

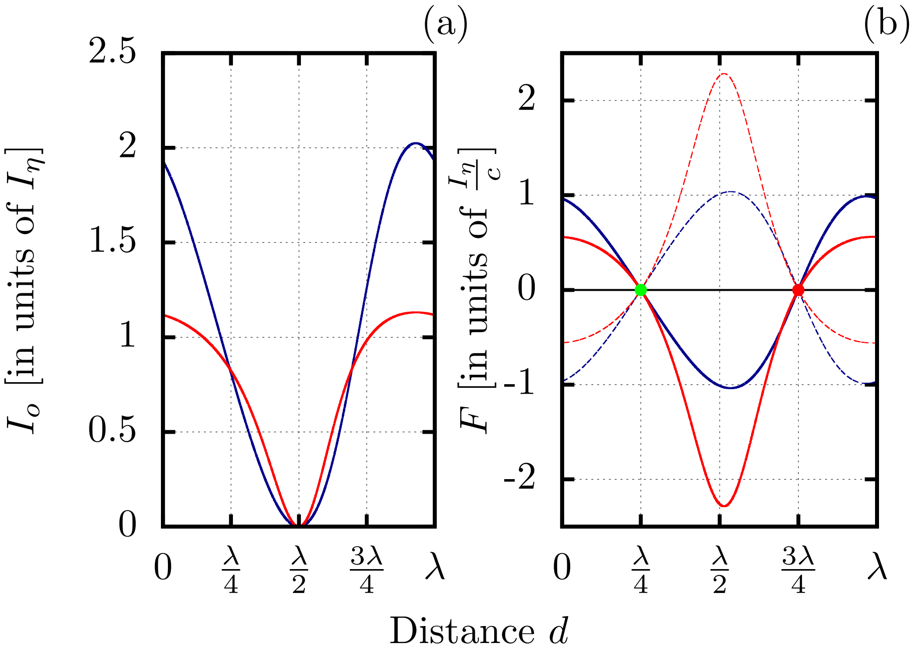

Figure 4.13: Fig. a) shows the outgoing intensities I_{ol} (solid line) and I_{or} (dashed line) as function of distance d for only transverse pump, thus $I_l = I_r = 0$.
Fig. b) shows the forces on two beam-splitters as function of distance d for only transverse pump. The solid lines demonstrate the forces on the first beam-splitter and the dashed lines the forces on the second one. The red points are stable equilibria and the green ones not.
The blue lines correspond to $\zeta = 1/9$, the red lines to $\zeta = 1/9 + i/2$.
An imaginary part of ζ leads to a decrease in the intensity, as a consequence of absorption. It is interesting to see that an imaginary part of ζ enlarge the force on the particles. The force is stable at $d = 3\lambda/4$, independently of ζ.

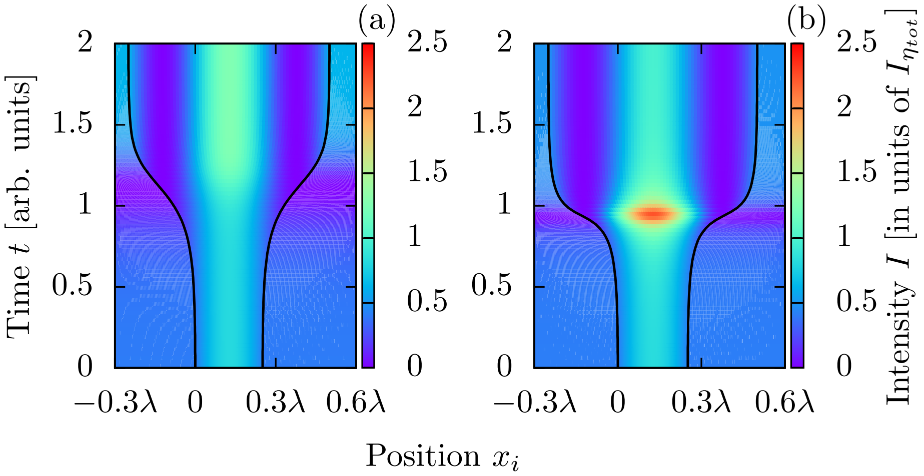

Figure 4.14: Two particles evolving over time with only transverse pump, $\zeta = 1/9$ (Fig. a)) and $\zeta = 1/9 + i/2$ (Fig. b)). They start at an unstable zero-point $d = \lambda/4$ and assemble at $d = 3\lambda/4$ after being numerically evolved. The intensity maxima is in the middle between the two particles.

shows some examples for the force on two particles. For the case with no longitudinal beams, because of symmetry, we do not have centre of mass motions. At $d = 3\lambda/4$ the scattered fields of the particles are 90 degrees out of phase and thus do not interfere. This is totally different to cavity induced self-ordering, where maximal collective scattering at exactly wavelength distance leads to the most stable configurations [12].Comparing Fig. 4.12b) with Fig. 4.13b), we see that the longitudinal beams change the stable distances and they depend stronger on ζ and on absorption.

Next we want to solve the motional dynamics of the two particle system subject to these forces numerically and take a look at how the particle positions evolve over time by solving the coupled equations of fields and particle motion. We introduce the procedure for these simulations in more detail later in the multiparticle case in section 4.3.2. This allows us to see, how the system finds equilibrium points as in Fig. 4.14, where we start from an unstable zero-point $d = \lambda/4$ and let the system evolve, which adjust a stable configuration at the equilibria point calculated in Eq. (4.23) $d = 3\lambda/4$.

Here the forces change the particle positions, which induces a change of the intensity over time. For the numerical simulations, we choose $I_{\eta_{tot}} = NI_\eta$, here $N = 2$, so that the intensity is comparable for different numbers of particles. Fig. 4.14 also shows that the two particles trap light between them. Although they in general should be attracted by high intensities, they do not assemble at the intensity maxima, but trap light between them. A similar behaviour is found for self-ordered solutions for the continuous Vlasov model for an ultracold gas in such a field [14].

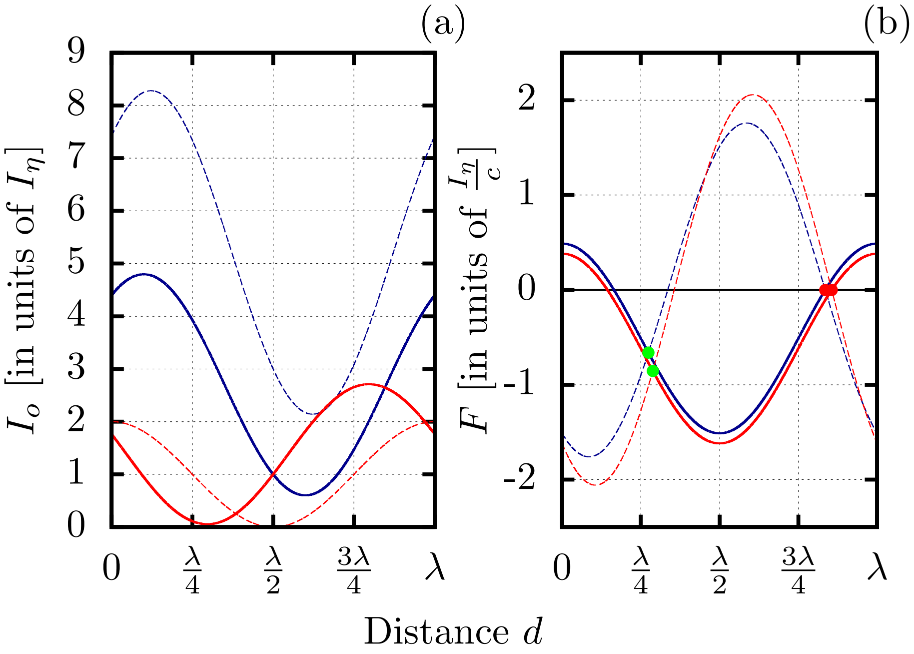

Figure 4.15: Intensity (Fig. a)) and force (Fig. b)) for a two particle system in the weak-coupling-limit, meaning $\zeta = 0$, for $I_r = I_\eta$. The blue line corresponds to $I_l = 3I_\eta$ and the red line to $I_l = 0$. In Fig. a) the solid line corresponds to the outgoing light to the left of the system and the dashed line to the one to the right of the system. Because of the high right incoming intensity, the blue dashed line is very high.
In Fig. b) the solid line shows the force on the first particle, and the dashed line on the second one. Red points are stable points.
Comparing this figure with Fig. 4.12, we see that the force for this case is lower, as a consequence of the fact, that ζ is proportional to the optical forces.

Two particles in the vanishing coupling limit $\zeta = 0$

As a special case, we introduce the very weak-coupling-limit. In this section we only treat this case for two particles. Later in this work we examine this limit for larger systems of particles (section 4.3.1). In this limit we neglect $\zeta = 0$, but still keep finite scattering into the fibre. Remembering $\zeta = -ir/t$, we see that this means that no light is reflected, but all transmitted through each of the particles acting as a beam-splitter. Reminding the definition of the coupling constant ζ Eq. (2.12) and that $\eta \propto \tilde{\alpha} \cdot \mathbf{E}_{loc}^2$, we see that coupling constant and transverse pump η are both proportional to the polarizability [39]. In principle we have to compensate a small η with a stronger transverse pump. For this case the intensities look as follows:

$$I_{ol} = I_\eta \left(1 + \cos(kd)\right) + I_r + \sqrt{2 I_\eta I_r} \left(\cos(kx_1) + \cos(k(x_1 + d))\right), \tag{4.24}$$

$$I_{or} = I_\eta \left(1 + \cos(kd)\right) + I_l + \sqrt{2 I_\eta I_l} \left(\cos(kx_1) + \cos(k(x_1 + d))\right). \tag{4.25}$$

As a consequence of the fact that no light is reflected, the outgoing light on the left side only depends on the incoming light from right and the scattered light. This phenomenon is also shown in Fig. 4.15a).
Next we calculate the forces:

$$F_1 = I_\eta \cos(kd) + \sqrt{2 I_\eta} \left(\sqrt{I_r} - \sqrt{I_l}\right) \cos(kx_1), \tag{4.26}$$

$$F_2 = -I_\eta \cos(kd) + \sqrt{2 I_\eta} \left(\sqrt{I_r} - \sqrt{I_l}\right) \cos(k(d + x_1)). \tag{4.27}$$

Fig. 4.15b) shows some example for the force in the weak-coupling-limit.
To enable finding the equilibrium points, we choose the position of the first particle at $x_1 = 0$ and do not care about centre of mass motions. So the stable distances read:

$$kd = -\arccos\left(\frac{\sqrt{I_r} - \sqrt{I_l}}{-\sqrt{2 I_\eta} + \sqrt{I_r} - \sqrt{I_l}}\right) + 2\pi n, \text{ if } \sqrt{I_r} - \sqrt{I_l} < \sqrt{\frac{I_\eta}{2}}. \tag{4.28}$$

By setting $x_1 = 0$, we find that there do only exist solutions for higher left than right incoming intensity or for small differences between I_l and I_r.

4.2.2 Three Particles

In this section we add a third particle but still have no injected fields $I_l = I_r = 0$. As mentioned above, the analytic results can be calculated here, but are very complicated, thus we only show some special cases and only write the intensity for $\zeta \in \Re$ and the

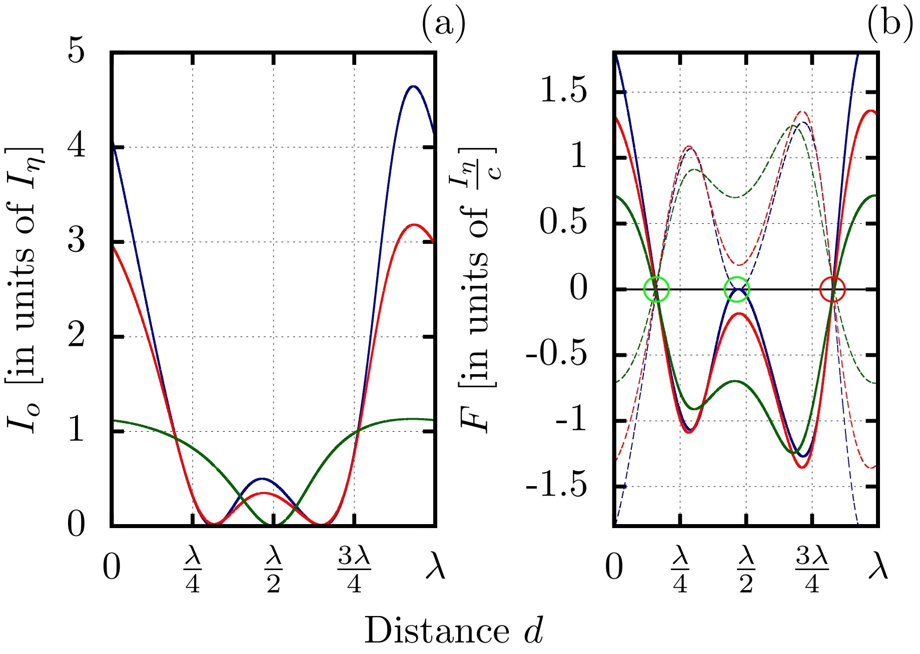

Figure 4.16: Intensity (Fig. a)) and forces (Fig. b)) of three beam-splitters without longitudinal beams, thus $I_l = I_r = 0$ and equal distances $d_1 = d_2 = d$. The blue line corresponds to $\zeta = 1/9$, the red line to $\zeta = (1+i)/9$ and the green one to $\zeta = 1/9 + i/2$. Fig. a) The imaginary part of ζ reduces the outgoing intensities as we have already seen for the single and two particle problem.
Fig. b) Solid lines correspond to the first beam-splitter and dashed lines to the third one. At the red points the configurations are stable and at the green ones not. Because of symmetry the force on the second particle F_2 is zero and the other two fulfil $F_1 = -F_3$. While the blue line has three zero-points per wavelength, the other ones have only two. So the imaginary part of ζ reduces the number of zero-points. It is also interesting that the stable point at $d \approx 4\lambda/5$ does not depend much on ζ.

forces for small ζ. With equal distances $d_1 = d_2 = d$, where d_1 is the distance between the first two particles and d_2 between the second and the third one, we get for the outgoing intensities:

$$I_{ol} = I_{or} =$$
$$\frac{I_\eta(1+\zeta^2)}{2}\left|\frac{1+2\cos(kd)-2\zeta\sin(kd)}{(i+3\zeta)\cos(kd)+(1-\zeta(i+2\zeta))\sin(kd)}\right|^2, \tag{4.29}$$

which again includes $I_{ol} = I_{or}$ for reasons of symmetry. For $\zeta \to 0$ the intensities converge to $I \simeq I_\eta/2\,|1+2\cos(kd)|^2$ which can lead up to nine times stronger collective scattering than for a single particle. Some examples for the outgoing intensities and the forces are shown in Fig. 4.16.

Assuming small ζ and neglecting terms of $O(\zeta^2)$ or higher, we get:

$$F_1 \simeq \frac{I_\eta}{c}\left(\cos(kd)+\cos(2kd)-\zeta(2\sin(2kd)+\sin(3kd)+\sin(4kd))\right)+O[\zeta]^2. \tag{4.30}$$

Symmetry implies $F_1 = -F_3$ and $F_2 = 0$. For this symmetric case, we get stable configurations at about $d \approx 4\lambda/5$, which does not depend much on ζ, as shown in Fig. 4.16.

Although we also allow for solutions with $d_1 \neq d_2$ in Fig. 4.17, the only stable solutions are given on the line, where $d_1 = d_2$ and for the chosen parameters there do not exist points, where all forces are equal for the asymmetric case. The stability of such points can easily be checked by calculating the derivation.

Fig. 4.18 shows the time evolution of the particle positions for three particles. Again the particles tend to trap light. The beam-splitter in the middle arranges at an intensity maximum.

4.2.3 Four Particles

As analytical results are getting more and more complicated for larger systems, we just take a short look at the system with four particles. So we just plot the intensity in Fig. 4.19 and the forces in Fig. 4.20. The transfer-matrix for this system can be calculated by:

$$M = M_{BS}\cdot P(d_1)\cdot M_{BS}\cdot P(d_2)\cdot M_{BS}\cdot P(d_3)\cdot M_{BS}. \tag{4.31}$$

Fig. 4.20 shows the forces on four particles for different ζ. It is interesting that a larger imaginary part of ζ reduces the number of zero-points for the force. It is more difficult to find zero-points for this case. Hence, in Fig. 4.20 do not exist stable cases with $d_1 = d_2 = d_3$. Investigating the case for different distances between the particles in Fig. 4.21, the particles form symmetric configurations with $d_1 = d_3 \neq d_2$.

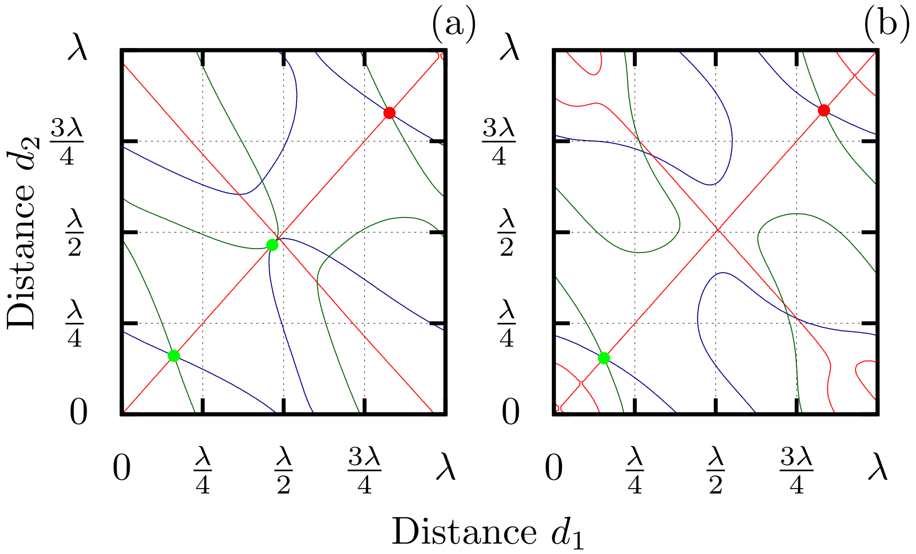

Figure 4.17: Contour lines of zero force F_1 (blue), F_2 (red) and F_3 (green) as function of the distance between the beam-splitters one and two d_1 and the beam-splitters two and three d_2 for $I_l = I_r = 0$, $\zeta = 1/9$ (Fig. a)) and $\zeta = 1/9 + i/2$ (Fig. b)). The red points show stable points and the green ones unstable equilibria. It is interesting that one of the unstable zero-points vanishes when we add an imaginary part to ζ as we have already seen in Fig. 4.16b).

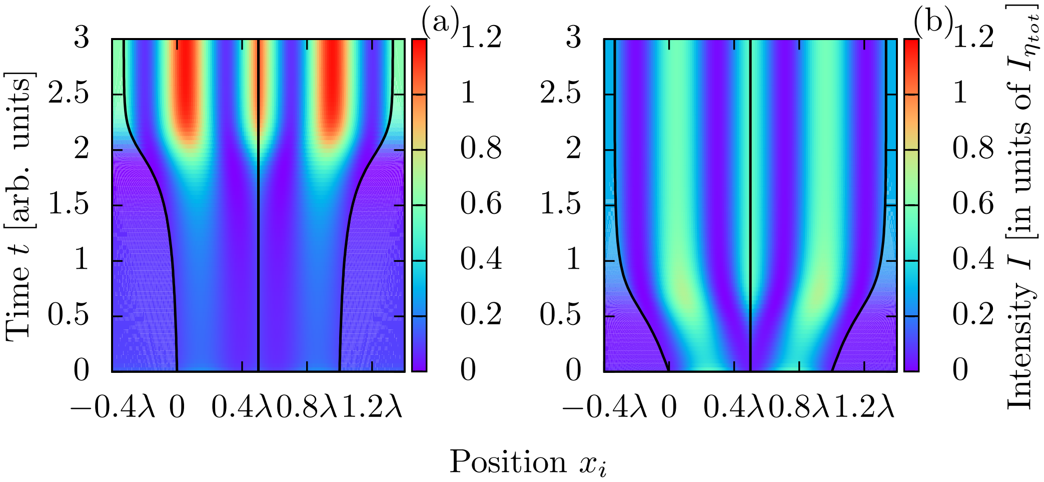

Figure 4.18: Three particles evolving over time with only transverse pump, $\zeta = 1/9$ (Fig. a)) and $\zeta = 1/9 + i/2$ (Fig. b)). They start at an unstable point $d = \lambda/2$ and arrange at about $d \approx 4\lambda/5$ after being numerically evolved. There is an intensity maximum in the middle of both particle neighbour pairs. In this case the beam-splitter in the middle assembles at an intensity maximum. Without imaginary part of ζ this intensity maxima is even higher. With imaginary part of ζ the particles reorder faster than without ζ_i. The reason is that for only real ζ, exists an unstable zero-point at $d \approx \lambda/2$.

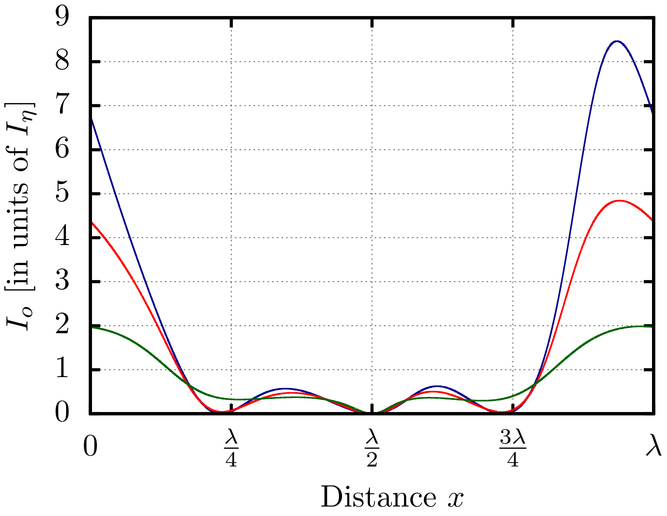

Figure 4.19: Outgoing intensity for a system with four beam-splitters as function of the distance $d_1 = d_2 = d_3 = d$ with $I_l = I_r = 0$. The blue line corresponds to $\zeta = 1/9$, the red line to $\zeta = (1 + i)/9$ and the green line to $\zeta = 1/9 + i/2$. As expected for the symmetric case is again $I_{ol} = I_{or}$. The intensity maxima decrease for higher imaginary part of ζ.

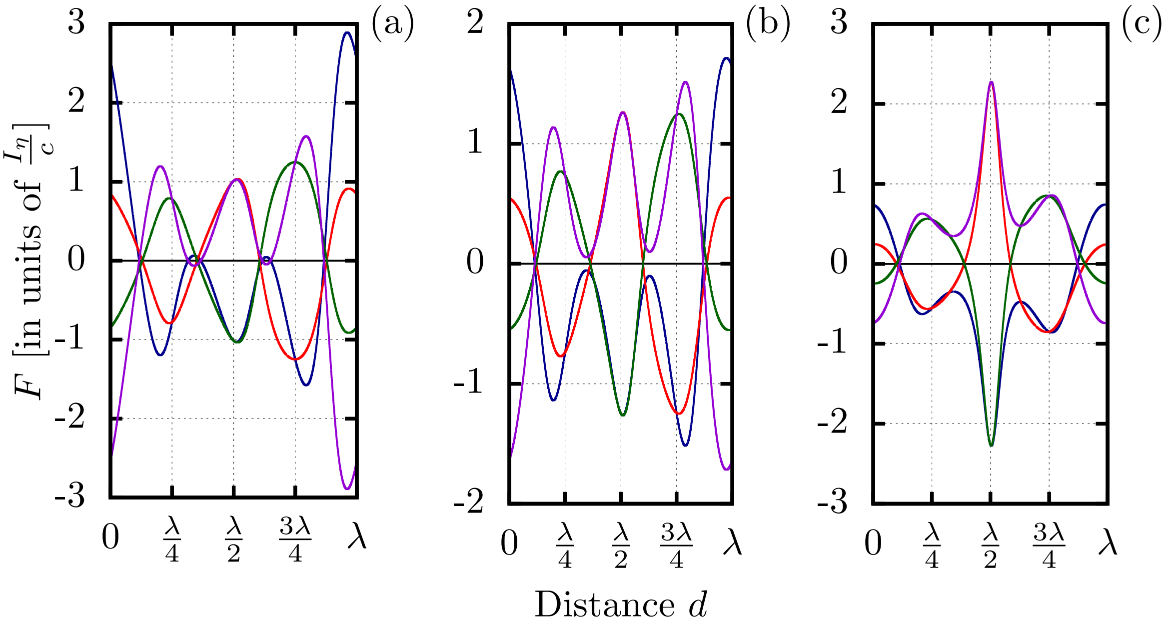

Figure 4.20: Forces on four particles as function of the distance $d_1 = d_2 = d_3 = d$ with $I_l = I_r = 0$. Fig. a) shows the forces for $\zeta = 1/9$, Fig. b) for $\zeta = (1+i)/9$ and Fig. c) for $\zeta = 1/9 + i/2$. As expected $F_1 = -F_4$ and $F_2 = -F_3$.
An imaginary part of ζ reduces the number of zero-points for the single forces. For these cases we can not find any equilibrium points with $d_1 = d_2 = d_3 = d$.

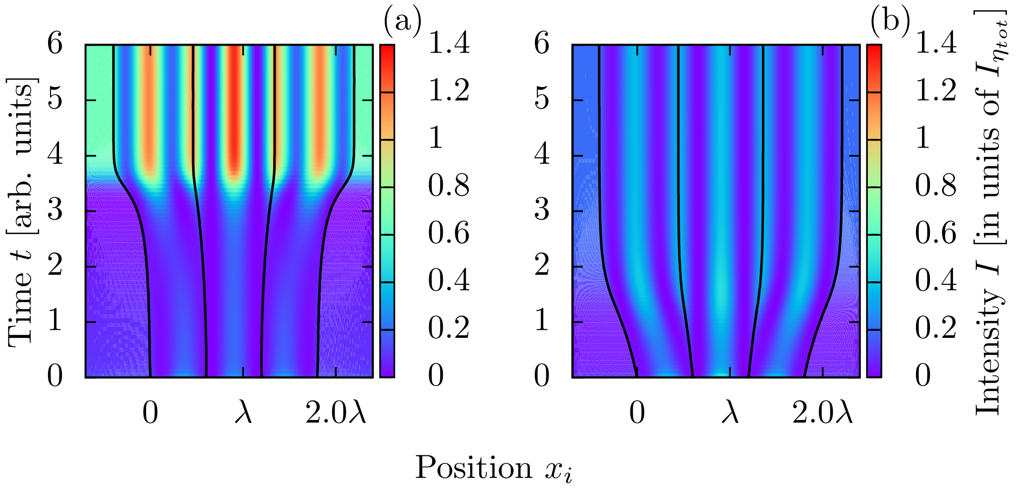

Figure 4.21: Four particles evolving over time with only transverse pump, $\zeta = 1/9$ (Fig. a)) and $\zeta = 1/9 + i/2$ (Fig. b)). They start at an unstable point $d = 0.6\lambda$ and assemble at a stable position after being numerically evolved. There are intensity maxima in the middle of all particle neighbour pairs. The two particles in the middle propagate on an intensity maximum. In this case without imaginary part of ζ these intensity maxima are even higher. The distances between the first two and the last two particles are equal, while the two particles in the middle have different distances.

4.3 Dynamics of larger particle ensembles

4.3.1 Weak-scattering-limit $\zeta = 0$

In their pioneering work Chang and coworkers [15] predicted regular spaced solutions for two-level atoms in the negligible coupling limit, meaning $\zeta = 0$. In this limit the field rescattered by the atoms is negligible. When we solve this system for a larger ensemble of particles, for equidistant ordering $d_1 = d_2 = \cdots = d_{N-1} = d$, we can calculate the transfer-matrix of the whole system easily in the form:

$$M = (M_{BS} \cdot P(d))^{N-1} \cdot M_{BS}. \tag{4.32}$$

For the scattered intensities we then get the rather simple expression:

$$I_{ol} = I_{or} = \frac{I_\eta}{2} \left(\frac{\sin(\frac{Nkd}{2})}{\sin(\frac{kd}{2})} \right)^2 . \tag{4.33}$$

This reminds of scattering from a regular grating. Some examples for the intensity are shown in Fig. 4.22.

Also the force on the m-th particle of N beam-splitters can be obtained in closed form

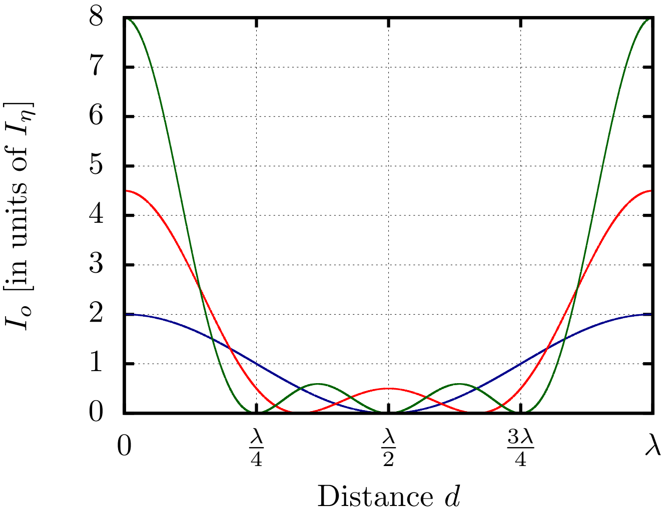

Figure 4.22: Outgoing intensities for two (blue), three (red) and four (green) particles for vanishing $\zeta = 0$. Again is true $I_{ol} = I_{or}$. The outgoing intensities come from the transverse pump transmitted through the particles without reflection.

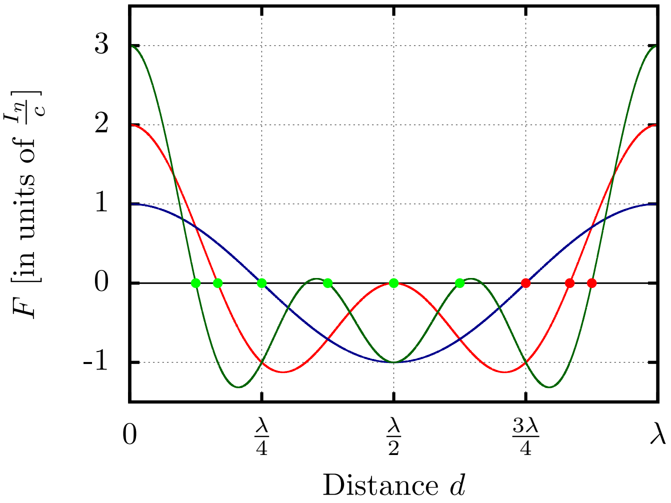

Figure 4.23: Force on the first of two (blue), three (red) and four (green) particles for vanishing $\zeta = 0$. Red dots denote stable equilibrium points. The more particles we add, the more zero-points per wavelength we get. The system can only be stable, when the outermost particle is at a stable position. In this figure the outermost particles are stable at the equilibrium point $d = (2N - 1)/(2N)$.
The zero-points of four particles, which we did not mark, are not representing stationary states, because they do not exist for all four beam-splitters.

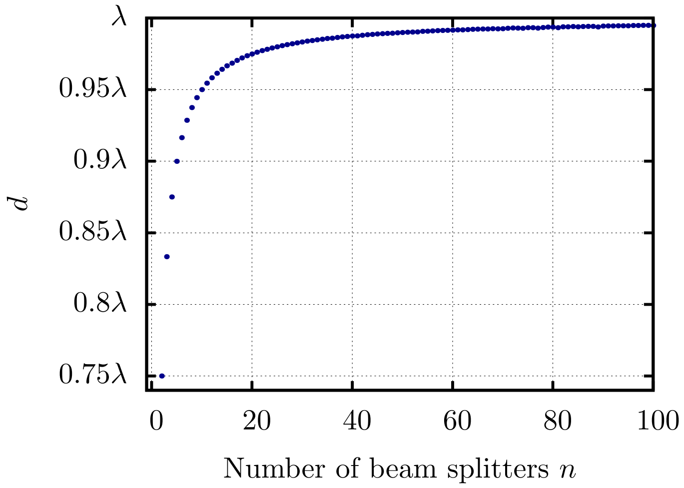

Figure 4.24: Stable distance as function of number of beam-splitters N, numerically solved with initial condition $d_0 = \lambda$ for $\zeta = 0$ and $I_l = I_r = 0$. The particles adjust a stable configuration with $d = (2N-1)/(2N)\lambda$.

to give

$$F_m = -\frac{I_\eta \cos(Nkd/2)\sin((2m-N-1)kd/2)}{c\sin(kd/2)}. \tag{4.34}$$

The zero-points of this force look:

$$d = \frac{2n-1}{2N}\lambda, \text{with } n \in \mathbb{N}. \tag{4.35}$$

With this we get a regular, equally spaced distribution of scatterers. Adding a particle also means, getting a new zero-point as shown in Fig. 4.23. Since it is not easy to check for stability, we try to find the stable zero-points numerically as shown in Fig. 4.24. Although we have a large number of zero-points, the only stable points are at $n = N$ and at equal distance between all particles $d_1 = d_2 = \cdots = d_{N-1} = d$:

$$d = \frac{2N-1}{2N}\lambda. \tag{4.36}$$

Within this limit every particle interacts equally strong with all the other particles via the fibre field. This nicely reproduces the results found by Chang by a very different approach [15].

In the next section we examine this case with finite ζ, including absorption and see, how the behaviour of the system changes.

4.3.2 Numerical simulations for large ensembles

In this section we treat systems with a larger number of particles. As such systems can hardly be solved analytically, we concentrate on numerical solutions.

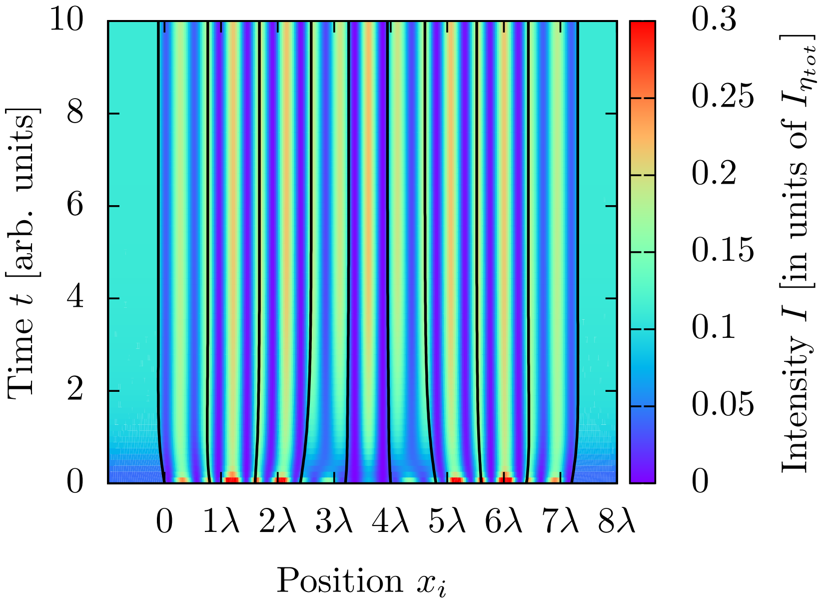

Figure 4.25: Trajectories of ten beam-splitters for $I_l = I_r = 0$ with initial condition $d_1 = d_2 = \cdots = d_9 = 0.8\lambda$ and $\zeta = (1+i)/9$. Note that the outermost particles are not trapped at intensity nodes or antinodes as would be expected from a conventional lattice.

We add a mass m to the beam-splitter and a friction coefficient μ to the environment to stabilize the system. Then we evolve the system over time by integrating Newton's equation $m\ddot{x}_j = -\mu\dot{x}_j + F_j(x_1, \cdots, x_N)$ until an equilibrium state is reached. Assuming the over-damped limit, where the second term dominates the first one, for example plastic beads in water, the velocity is determined by:

$$\dot{x}_j = \frac{F_j(x_1, \cdots, x_N)}{\mu}. \tag{4.37}$$

So we start from a special position and calculate the electric fields to the left and to the right of the system using the transfer-matrix-method. With this we can compute the force on the particles and find the new positions, after every step. Without damping the trapped clouds experience a harmonic restoring force, when being small displaced. From this we get the characteristic time, the oscillation period of a single trapped cloud τ_{osc}. In the overdamped limit the particles reach the velocity F/μ during the short time $\tau_{vel} = m/\mu$, with $\tau_{vel} \ll \tau_{osc}$, so that the system does not perform many oscillations before forming a final configuration. [6]

Fig. 4.25 shows the coupled atom-field dynamics for an example for ten particles, starting at a regular distance $d = 0.8\lambda$. The particles move and reorder at new distances, which are not equidistant, but mirror symmetric, meaning $d_1 = d_8$, $d_2 = d_7$ and so on. The inner particles order close to intensity maxima, while the outer particles are shifted from local intensity maxima. The outer particles in this case behave like mirrors,

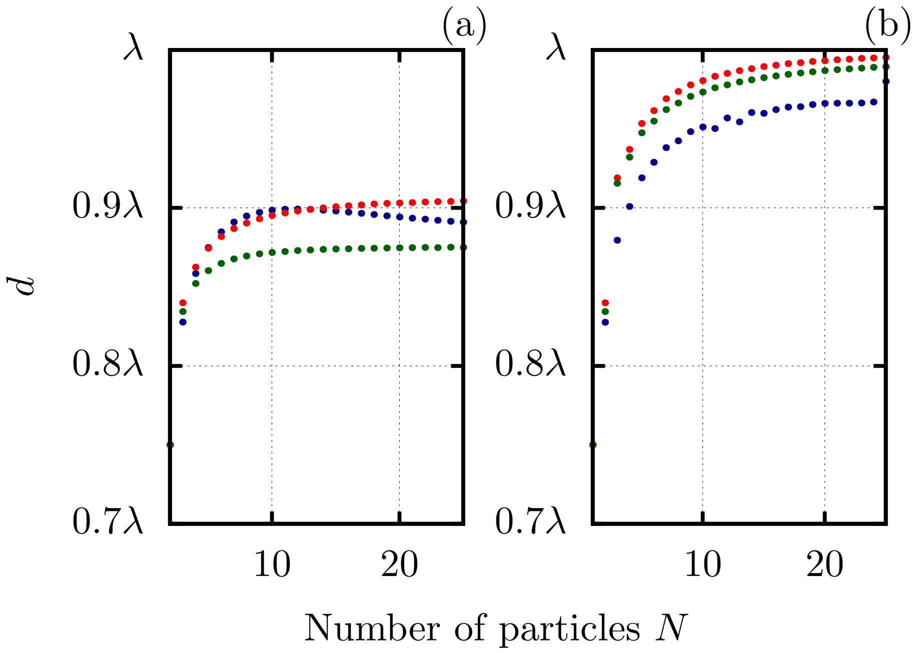

Figure 4.26: Stable distances d_1 (Fig. a)) and $d_{N/2}$ for a even number, respectively $d_{(N+1)/2}$ for a odd number of particles (Fig. b)) as function of number of beam-splitters N, numerically solved with initial condition $d_0 = \lambda$. The red lines correspond to $\zeta = 1/9$, the blue lines to $\zeta = i/2$ and the green lines to $\zeta = 1/9 + i/2$. It seems as if the imaginary part of ζ reduces the distance of the particles in the middle, while a real part enlarges it. The particles in the middle arrange at a larger distance than the outermost particles.

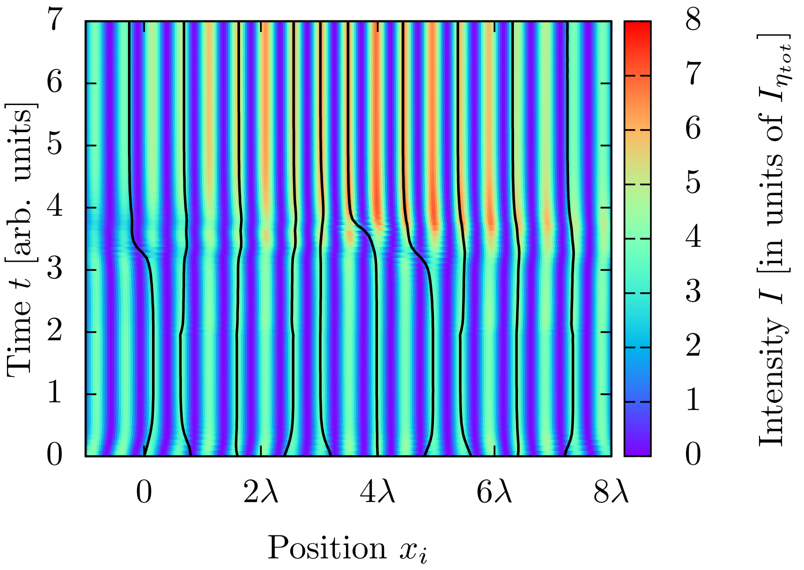

Figure 4.27: Trajectories of ten beam-splitters for $I_l = I_r = I_{\eta_{tot}}$, $\zeta = 1/9$ and $\phi = 0$ with initial condition $d_1 = d_2 = \cdots = d_9 = 0.8\lambda$. For the first three time-steps $I'_{\eta_{tot}} = 0$, then $I_{\eta_{tot}} \neq 0$. It can be observed that the particles reorder in a new stable configuration when we switch on the transverse pump at $t = 3$.

forming a resonator, which capture high field intensities between them. Choosing a higher number of particles, the distances are only slightly modified as we can see in Fig. 4.26. While the stable position of two particles with no longitudinal beams does not depend on ζ, it does for higher number of particles. We plot the distances of the first two particles and of two particles in the middle of the configuration in Fig. 4.26. First the distances grow until they reach a stationary value below λ. We can also find stable configurations for high particle numbers and high absorption rates. In a qualitative way this agrees with the corresponding result obtained via the Vlasov approach in ref. [14]. It seems that the particles behave like a self-forming optical resonator trapping the scattered light in its centre. Such configurations tend to minimize the combined total potential energy of all the particles [41].

In the next step we examine the change of a stable configuration with and without a transverse pump. We first let the system settle to an equilibrium point in a prescribed standing wave. When the system reaches a stable position we switch on a transverse pump η instantaneously and watch how the system evolves. This behaviour is demonstrated in Fig. 4.27 and 4.28. The system in Fig. 4.27 first forms a self-consistent configuration in the standing wave. After switching on the transverse pump, the particles start to interact differently and reorder into a new equilibrium. This changes strongly when one introduces small absorptions as shown in Fig. 4.28. Then we get a configuration, which first is stable without transverse pump, but gets unstable after the switch on of the pump. Such a behaviour can also be found for very large conventional optical lattices

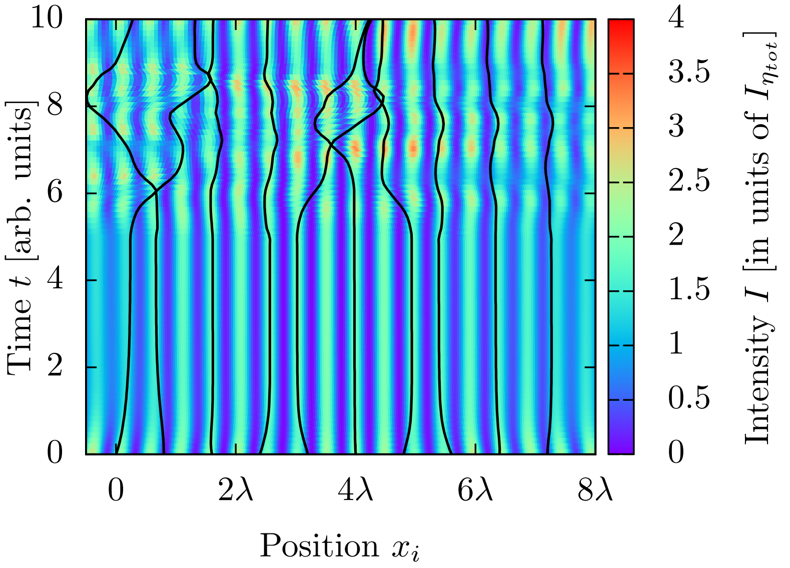

Figure 4.28: Trajectories of ten beam-splitters for $I_l = I_r = I = I_{\eta_{tot}}$, $\zeta = 1/9 + i/18$ and $\phi = 0$ with initial condition $d_1 = d_2 = \cdots = d_9 = 0.8\lambda$. For the first five time-steps $I'_{\eta_{tot}} = 0$, then $I_{\eta_{tot}} \neq 0$. As the particle trajectories begin to cross we see that the configuration gets unstable one the transverse pump is switched on.

and clearly demonstrates that we do not have conservative dynamics here.

We see that in the standing wave trap the particles order at the intensity maxima, but with transverse pump the outer particles again leave the intensity maxima and trap light between them.

Chapter 5

Self-ordering with asymmetric directional scattering amplitudes $\alpha \neq \beta$

Up to now, we have chosen $\alpha = \beta$, which means that the light from the transverse pump-laser is symmetrically scattered to the left and to the right. Now we want to examine cases, where this is no longer so. Using a transverse pump with a polarization, which is not aligned perpendicular to the fibre, we break the mirror symmetry of the set-up [39]. We model this behaviour by parametrizing the part of η reflected to the left as $\alpha = \sin(\theta)$ and the part reflected to the right as $\beta = \cos(\theta)$, fulfilling the condition $\alpha^2 + \beta^2 = 1$. Although α, β could be imaginary, we choose them here as real numbers. We again start with few particles, which allows analytical results and then enlarge our system, proceeding to numerical results.

5.1 One particle

First we again discuss this case for a single particle. Here, the outgoing field intensities are:

$$\begin{aligned} I_{ol} &= \frac{\left|\left(\sqrt{I_r} + \sqrt{I_l} e^{i(\phi+2kx)} i\zeta\right) + e^{ikx}\sqrt{I_\eta}(1-i\zeta)\sin(\theta)\right|^2}{1+|\zeta|^2}, \\ I_{or} &= \frac{\left|\left(\sqrt{I_l} e^{i(\phi+2kx)} + \sqrt{I_r} i\zeta\right) + e^{ikx}\sqrt{I_\eta}(1-i\zeta)\cos(\theta)\right|^2}{1+|\zeta|^2}. \end{aligned} \tag{5.1}$$

Typical behaviour for the scattered light with different θ can be seen in Fig. 5.1.

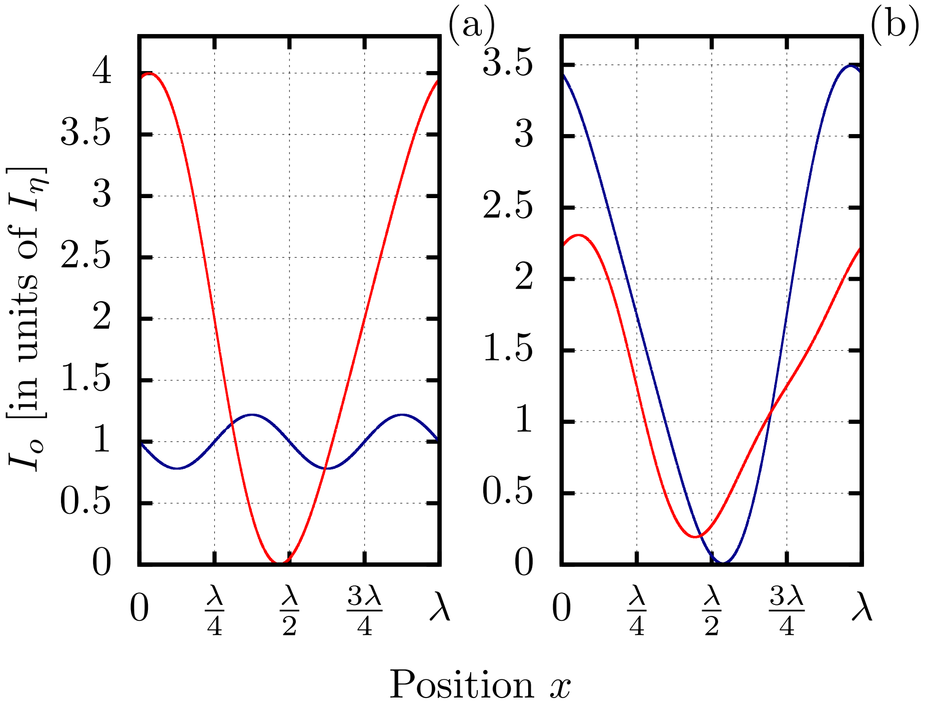

Figure 5.1: Outgoing intensities as a function of the position of the particle x for $I_l = I_r = I_\eta$, $\zeta = 1/9$ and $\phi = 0$. The blue line shows the outgoing intensities to the left and the red line to the right of the beam-splitter.
Fig. a) corresponds to $\theta = 0$, which means $\alpha = 0$ and $\beta = 1$, so all the light of the transverse pump is scattered to the right.
Fig. b) corresponds to $\theta = \pi/3$, which means $\alpha \approx 0.866$ and $\beta = 0.5$, so more light of the transverse pump is scattered to the left.
Hence in Fig. a) the outgoing intensity to the right reaches higher maxima, while in Fig. b) the outgoing intensity to the left does.
The zero-points at $x = \lambda/4$ and $x = 3\lambda/4$ also occur for symmetric pumping.

The force on the mirror then is non-zero even for $I_l = I_r = 0$ and reads:

$$
\begin{aligned}
F = {} & \frac{(I_l - I_r)\left(|\zeta|^2 + \zeta_i\right) - 2\sqrt{I_l I_r}\zeta_r \sin(2kx)}{\frac{c}{2}|1 - i\zeta|^2} \\
& + \frac{I_\eta}{c}(\alpha^2 - \beta^2) \\
& + \frac{2\sqrt{I_\eta I_l}}{c}\Re\left(\frac{i\alpha\zeta - \beta}{1 - i\zeta}e^{i(kx+\phi)}\right) \\
& + \frac{2\sqrt{I_\eta I_r}}{c}\Re\left(\frac{\alpha - i\beta\zeta}{1 - i\zeta}e^{-i(kx-\phi)}\right).
\end{aligned}
\tag{5.2}
$$

For $\alpha = \beta$ we recover Eq. (4.3) and see that we get an additional term. The second term represents the radiation pressure force induced by asymmetric scattering of the transverse pump light into the fibre. Also the interference terms between scattered and longitudinal fields, the third and the fourth term, are influenced by choosing asymmetric pump. Obviously we can only get stable positions for asymmetric scattering, if $I_l, I_r \neq 0$. By choosing $I_l, I_r \neq 0$, we can even get zero-points for high asymmetries as in Fig. 5.2 and 5.3.

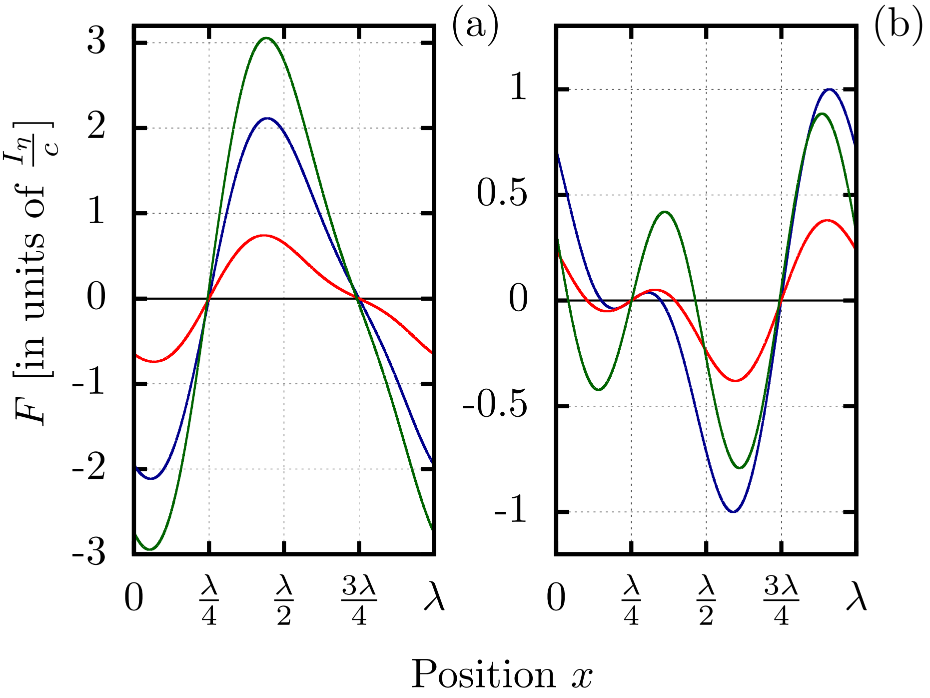

Figure 5.2: Force F on one beam-splitter for $\phi = 0$. The blue line corresponds to $I_l = I_r = I_\eta$ and $\zeta = 1/9$, the red line to $I_l = I_r = I_\eta$ and $\zeta = 1/9 + i/2$ and the green line to $I_l = 2I_\eta$, $I_r = I_\eta$ and $\zeta = 1/9$, for
(a) $\theta = 0$, and
(b) $\theta = \pi/3$.
Although we even get zero-points for high asymmetries, the number of zero-points per wavelength is higher, when choosing small asymmetries as in Fig. b). Comparing this figure with Fig. 5.3, we see, that for special θ, we can find a higher number of zero-points.

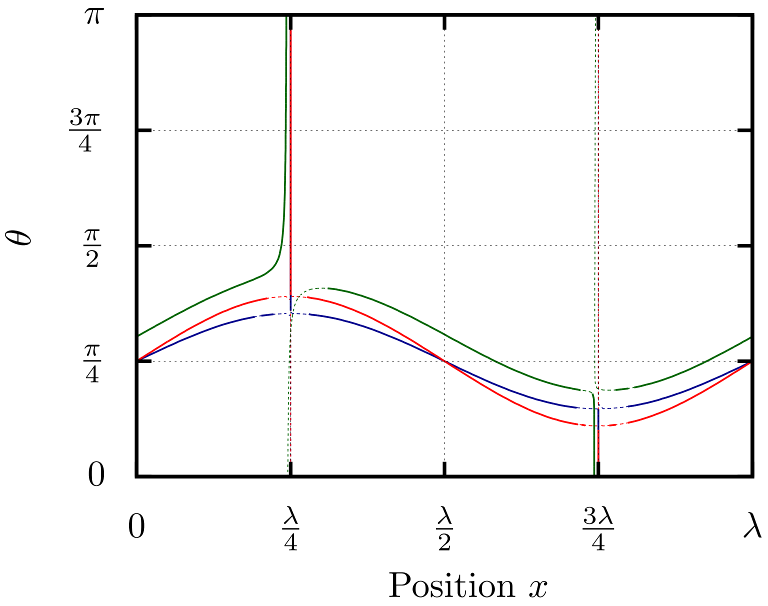

Figure 5.3: Zero-points of the force F on one beam-splitter for $\phi = 0$. The blue line corresponds to $I_l = I_r = I_\eta$ and $\zeta = 1/9$, the red line to $I_l = I_r = I_\eta$ and $\zeta = 1/9 + i/2$ and the green line to $I_l = 2I_\eta$, $I_r = I_\eta$ and $\zeta = 1/9$.
Solid lines correspond to stable points. As we have already seen in Fig. 5.2, high asymmetries reduce the number of zero-points per wavelength. In the region around $\theta = \pi/4$ there are four zero-points per wavelength, and outside of this region only two.
For $I_l = I_r$ (blue and red lines) we get zero-points at $x = \lambda/4$ and $x = 3\lambda/4$, independently of ζ and θ. For small ζ the position at $x = 3\lambda/4$ is stable, until new zero-points around $\theta \approx \pi/4$ appear. For larger θ, when this additional zero-points vanish, $x = \lambda/4$ is stable.

5.2 Multiparticle dynamics with asymmetric scattering

For the multiparticle case, we again set $I_l = I_r = 0$. Introducing asymmetric transverse pump, changes the interaction properties of the particles in the system. For two particles we do not get forces of equal magnitude any more, which leads to a final centre of mass motion. Nevertheless, we look for configurations, where the forces on the particles are equal. This generates thus a propulsion of a pair of particles while keeping equal distance. Very similar behaviour was seen in experiments with silicon beads [42].

Some examples of this behaviour are demonstrated in Fig. 5.4. Comparing this figure with Fig. 4.13, we see that for the asymmetric case, the stability of the particles is not as strong as for the symmetric case. This behaviour can be determined by looking at the derivative of the forces. Especially for the $\theta = 0$-case the derivative of the first beam-splitter is approximately zero, but we can even find equilibrium points for such a strong asymmetry. Although the forces are equal on both particles for all three cases, we have a remaining centre of mass motion. That behaviour is also shown in Fig. 5.6, where we plotted the time dependent positions of two particles with asymmetric pump. The particles are moving toward a particular direction, determined by the asymmetric scattering. Again, the particles tend to confine much of the scattered light between them. The same effect is seen for three and four particles in Fig. 5.7. Although the forces change, the zero-points does not depend much on θ for low absorption as shown in Fig. 5.5.

As a last part we want to examine the time evolution of a larger system with asymmetric scattering. Fig. 5.8 demonstrates an unstable system with ten particles. First the particles start to oscillate around a stable point, and then the system gets unstable after a while. This behaviour is a consequence of the small derivative of the force as we have already seen for two beam-splitters.

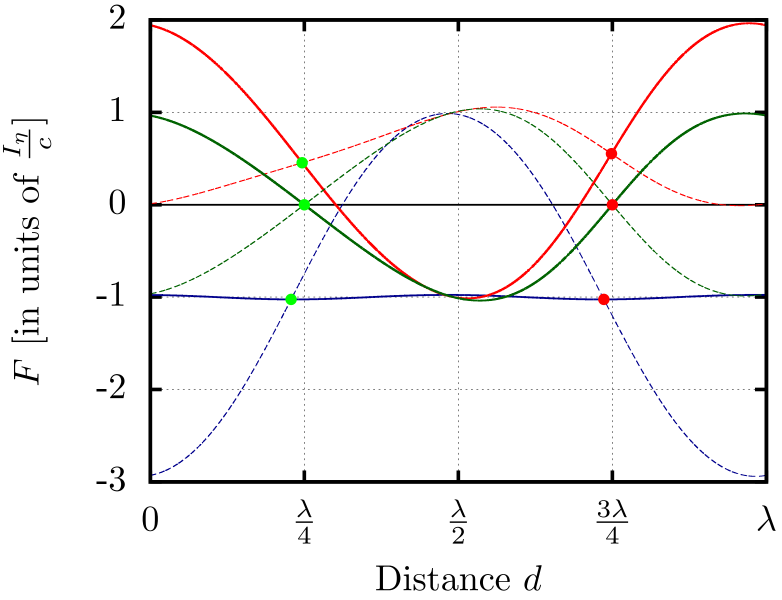

Figure 5.4: Force on two beam-splitters as function of the distance d for $I_l = I_r = 0$ and $\zeta = 1/9$ with scattering asymmetries. The blue line corresponds to $\theta = 0$, the red line to $\theta = \pi/3$ and the green line to $\theta = \pi/4$. The solid line shows the force on the first beam-splitter and the dashed line the force on the second beam-splitter. Crossings of the lines with equal force on the two particles here also occur non-zero force values. The red points are stable distances, while the green ones are not.
The absolute value of the derivative of the forces for $\theta \neq \pi/4$ is not as large as for the symmetric case, thus the stability is not as strong as for the $\theta = \pi/4$-case.

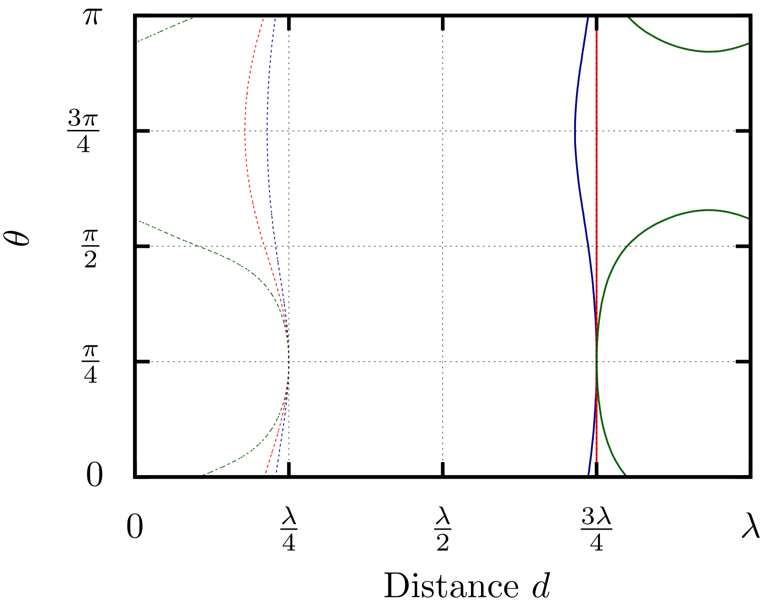

Figure 5.5: Equilibrium points of the force on two beam-splitters as function of the distance d and θ for $I_l = I_r = 0$. The blue line corresponds to $\zeta = 1/9$, the red line to $\zeta = (1+i)/9$ and the green line to $\zeta = 1/9 + i/2$. Solid lines show stable points. In contrast to the one particle case in Fig. 5.3, for a two particle system the number of equilibrium points for low absorption does not change with θ. Also the positions of the zero-points do not depend much on θ. The high absorption case (green line) is only stable for some θ's.

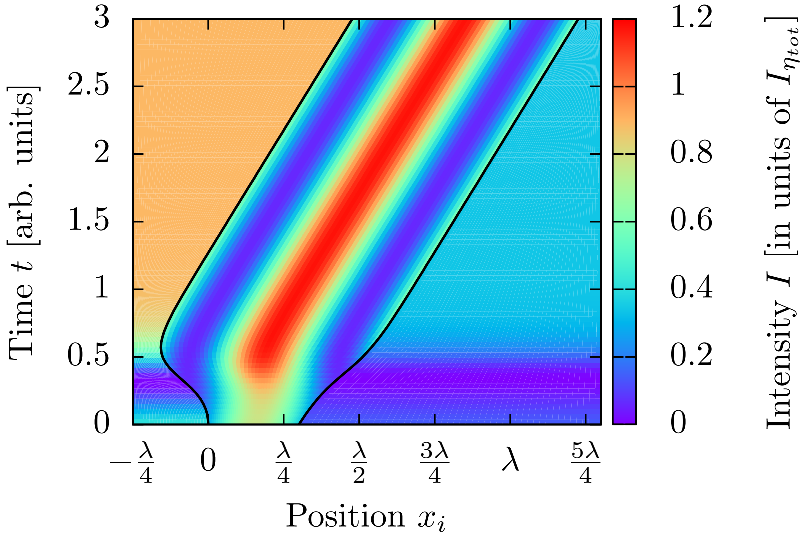

Figure 5.6: Trajectories of two beam-splitters for $I_l = I_r = 0$, $\zeta = 1/9$ and $\theta = \pi/3$ with initial condition $d = 0.3\lambda$. We see that the particles are pushed to the right because of the scattering asymmetry, but they keep a stable final distance. Again the intensity maximum is between them.

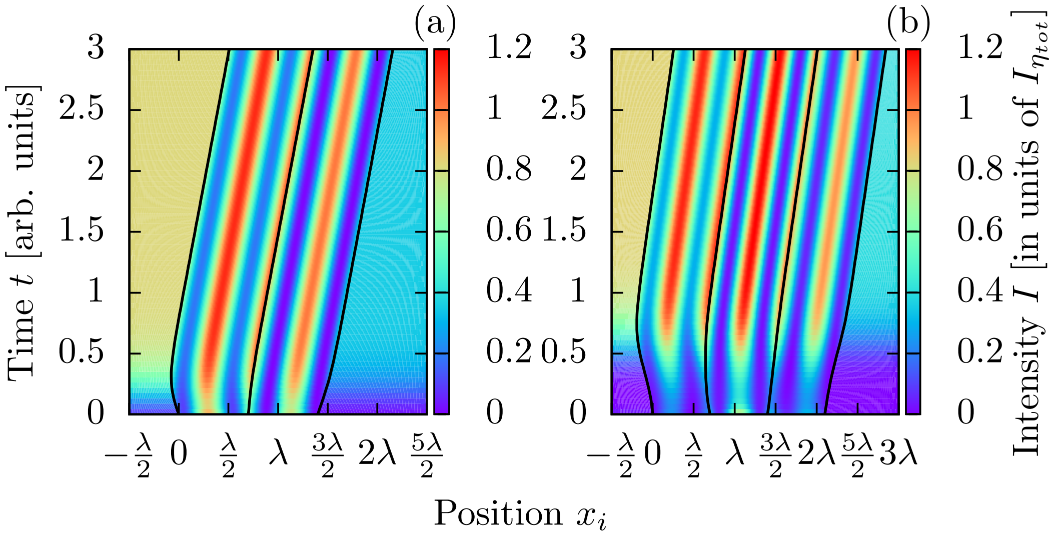

Figure 5.7: Trajectories of three (Fig. a)) and four beam-splitters (Fig. b)) for $I_l = I_r = 0$, $\zeta = 1/9$ and $\theta = \pi/3$ with initial condition $d = 0.7\lambda$. Also these particles are pushed to the right, but keep a fixed distance. Independent of the particle number, the outer particles tend to trap light between them and some inner particles assemble at intensity maxima.

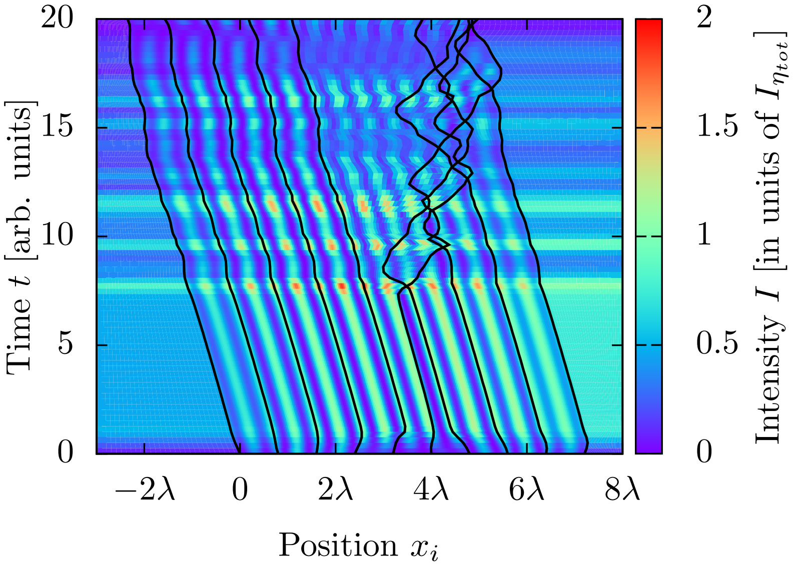

Figure 5.8: Trajectories of ten beam-splitters for $I_l = I_r = 0$, $\zeta = \frac{1}{9}$ and $\theta = \pi/5$ with initial condition $d_1 = d_2 = \cdots = d_9 = 0.8\lambda$. First the particles start to oscillate and then the system gets unstable.

Chapter 6

Conclusions

Using a conceptionally simple and intuitive classical scattering model, we studied the coupled atom-field-dynamic. Starting with symmetric scattering and a single particle, we observed that the configurations could only be stable, when the difference between left and right incoming intensities is not too large. Afterwards we examined the one particle case for small ζ and discovered that this threshold vanishes, as a consequence that ζ is proportional to the optical forces acting on the system. Investigating the particle in a standing wave with additional transverse pump shows that the transverse pump changes the periodicity of the force from $\lambda/2$ to λ. Then we chose only left incoming light with transverse pump and saw that I_η/I_l has to exceed a special threshold to guarantee stability.

For the two particle case we discovered that the particles are stable at distance $d = 3\lambda/4$, when setting $I_l = I_r = 0$. At this distance the scattered fields from the two particles do not interfere. Solving the weak coupling limit for N particles confirms the results found by Chang [15], namely $d = (2N-1)/(2N)$.

By adding more and more particles, finding zero points got more and more difficult, so we passed over to numerical solutions. Assuming the over-damped limit, which in an experiment could be provided by Doppler cooling or similar mechanisms, we let the system evolve over time. As the system is not conservative, the particles do not order at field maxima, corresponding to local potential minima, but at force zero points. So independently of the particle number, the outer particles tended to form a self-organized resonator confining high intensities of the scattered light between them, which was also found by [14] for a cold gas mean-field approach. So we have a sort of particle-based resonator without the need to artificially fix the particles [43]. In contrast to the longitudinal case such a configuration is not intrinsically unstable [41] as the destructive interference of scattered and propagating fields can stabilize the outermost particles.

It was also shown that larger particle numbers could lead to instabilities, as a consequence of the interference between the light scattered from the particles, which is the main contribution to the force.

We also observed that the distances between the particles grow for higher particle numbers until they reach a stable point.
At the end we chose asymmetric pump, where we saw that the particles can form configurations with fix distances, but still have a remaining centre of mass motion.
So we were able to include back-action and absorption, and to give an intuitive picture for the underlying microscopic dynamics.

Bibliography

[1] D. Jaksch, C. Bruder, J. I. Cirac, C. W. Gardiner, and P. Zoller. Cold bosonic atoms in optical lattices. *Phys. Rev. Lett.*, 81:3108–3111, Oct 1998.

[2] I.H. Deutsch, R.J.C. Spreeuw, S.L. Rolston, and W.D. Phillips. Photonic band gaps in optical lattices. *Physical Review A*, 52(2):1394, 1995.

[3] Gavin K. Brennen, Carlton M. Caves, Poul S. Jessen, and Ivan H. Deutsch. Quantum logic gates in optical lattices. *Phys. Rev. Lett.*, 82(5):1060, 1999.

[4] E. Vetsch, D. Reitz, G. Sagué, R. Schmidt, S.T. Dawkins, and A. Rauschenbeutel. Optical interface created by laser-cooled atoms trapped in the evanescent field surrounding an optical nanofiber. *Physical review letters*, 104(20):203603, 2010.

[5] Masao Takamoto, Feng-Lei Hong, Ryoichi Higashi, and Hidetoshi Katori. An optical lattice clock. *Nature*, 435(7040):321, 2005.

[6] J.K. Asbóth, H. Ritsch, and P. Domokos. Optomechanical coupling in a one-dimensional optical lattice. *Physical Review A*, 77(6):063424, 2008.

[7] Matthias Sonnleitner, Monika Ritsch-Marte, and Helmut Ritsch. Optomechanical deformation and strain in elastic dielectrics. *New Journal of Physics*, 14(10):103011, 2012.

[8] Matthias Weidemüller, Axel Görlitz, Theodor W. Hänsch, and Andreas Hemmerich. Local and global properties of light-bound atomic lattices investigated by bragg diffraction. *Physical review A*, 58(6):4647, 1998.

[9] G. Birkl, M. Gatzke, I.H. Deutsch, S.L. Rolston, and W.D. Phillips. Bragg scattering from atoms in optical lattices. *Physical review Letters*, 75(15):2823, 1995.

[10] J. Lee, D.H. Park, S. Mittal, M. Dagenais, and S.L. Rolston. Integrated optical dipole trap for cold neutral atoms with an optical waveguide coupler. *arXiv preprint arXiv:1303.2922*, 2013.

[11] A. Goban, K.S. Choi, D.J. Alton, D. Ding, C. Lacroûte, M. Pototschnig, T. Thiele, N.P. Stern, and H.J. Kimble. Demonstration of a state-insensitive, compensated nanofiber trap. *Physical Review Letters*, 109(3):33603, 2012.

[12] JK Asbóth, P Domokos, H Ritsch, and A Vukics. Self-organization of atoms in a cavity field: Threshold, bistability, and scaling laws. *Physical Review A*, 72(5):053417, 2005.

[13] Hilton W. Chan, Adam T. Black, and Vladan Vuletić. Observation of collective-emission-induced cooling of atoms in an optical cavity. *Physical review letters*, 90(6):063003, 2003.

[14] Tobias Grießer and Helmut Ritsch. Light induced crystallization of cold atoms in a thin 1D optical tube. *arXiv preprint arXiv:1303.7359*, 2013.

[15] D. E. Chang, J. I. Cirac, and H. J. Kimble. Self-organization of atoms along a nanophotonic waveguide. *Phys. Rev. Lett.*, 110:113606, 2013.

[16] S. Ostermann, M. Sonnleitner, and H. Ritsch. Scattering approach to two-colour light forces and self-ordering of polarizable particles. *New Journal of Physics*, 16(4):043017, 2014.

[17] André Xuereb, Claudiu Genes, and Aurélien Dantan. Collectively enhanced optomechanical coupling in periodic arrays of scatterers. *Physical review*, A 88(5):053803, 2013.

[18] André Xuereb, Peter Domokos, János Asbóth, Peter Horak, and Tim Freegarde. Scattering theory of cooling and heating in optomechanical systems. *Physical Review A*, 79(5):053810, 2009.

[19] J.D. Jackson. Classical electrodynamics. *John Wiley & Sons: New York*, 1998.

[20] Smith, King, and Wilkins. Optics and photonics. *Wiley*, 2007.

[21] J. Jahns. Photonik. *Oldenbourg*, 2001.

[22] L. Novotny and B. Hecht. Principles of nano-optics. *Cambridge*, 2006.

[23] V. V. Klimov and M. Ducloy. Spontaneous emission rate of an excited atom placed near a nanofiber. *Phys. Rev. A*, 69:013812, Jan 2004.

[24] Sho Chonan, Shinya Kato, and Takao Aoki. Efficient single-mode photon-coupling device utilizing a nanofiber tip. *Scientific Reports*, 4(4785):1707, 2014.

[25] R. Mitsch, C. Sayrin, B. Albrecht, P. Schneeweiss, and A. Rauschenbeutel. Directional nanophotonic atom–waveguide interface based on spin-orbit coupling of light. *arXiv preprint arXiv:1406.0896*, 2014.

[26] J. Dalibard and C. Cohen-Tannoudji. Dressed-atom approach to atomic motion in laser light: the dipole force revisited. *Optical Society of America*, 2(11), 1985.

[27] C. Cohen-Tannoudji. Atomic motion in laser light. In J.Dalibard, J.-M. Raimond, and J. Zinn-Justin, editors. *Fundamental Systems in Quantum Optics, Proceedings of the Les Houches Summer School, Sesion LIII*, pages 1–164, 1992.

[28] Mario Mützel. Erzeugung von Nanostrukturen mit laserpräparierten thermischen Atomstrahlen. *Dissertation zur Erlangung des Doktorgrades (Dr. rer. nat.) der Mathematisch-Naturwissenschaftlichen Fakultät der Rheinischen Friedrich-Wilhelms-Universität Bonn*, 2004.

[29] Hanspeter Helm. Dissipation der Licht-Atom Wechselwirkung: Realisierung und Anwendung der Laserkühlung von Atomen. *Vorlesungsunterlagen WS 06/07*, 2006.

[30] Bahaa E.A. Saleh and Malvin Carl Teich. Fundamentals of photonics. *John Wiley & Sons*, 1991.

[31] Fam Le Kien, J.Q. Liang, K. Hakuta, and V.I. Balykin. Field intensity distributions and polarization orientations in a vacuum-clad subwavelength-diameter optical fiber. *Optics Communications*, 242(4–6):445 – 455, 2004.

[32] Guillem Sagué Cassany. Cold atom physics using ultra-thin optical fibres. *Dissertation zur Erlangung des Doktorgrades (Dr. rer. nat.) der Mathematisch-Naturwissenschaftlichen Fakultät der Rheinischen Friedrich-Wilhelms-Universität Bonn*, 2008.

[33] Fam Le Kien and A. Rauschenbeutel. Propagation of nanofiber-guided light through an array of atoms. *arXiv preprint arXiv:1409.0346*, 2014.

[34] Rudolf Grimm and Matthias Weidemüller. Optical dipole traps for neutral atoms. *arXiv preprint arXiv:9902072*, 1999.

[35] J.-B. Béguin, E. Bookjans, S. L. Christensen, H. L. Sørensen, J.H. Müller, J. Appel, and E.S. Polzik. Generation and detection of a sub-poissonian atom number distribution in a one-dimensional optical lattice. *arXiv preprint arXiv:1408.1266*, 2014.

[36] A.V. Masalov and V.G. Minogin. Pumping of higher-order modes of an optical nanofiber by laser excited atoms. *Laser Physics Letters*, 10(7):075203, 2013.

[37] Ravi Kumar, Vandna Gokhroo, Aili Maimaiti, Kieran Deasy, Mary C. Frawley, and Síle Nic Chormaic. Interaction of laser-cooled ^{87}Rb atoms with higher order modes of an optical nanofiber. *arXiv preprint arXiv:1311.6860*, 2013.

[38] Sanli Faez, Pierre Türschmann, and Vahid Sandoghdar. High-cooperativity nanofibre laser. *arXiv preprint arXiv:1403.1885*, 2014.

[39] R. Mitsch, C. Sayrin, B. Albrecht, P. Schneeweiss, and A. Rauschenbeutel. Discerning and selectively manipulating laser-trapped atoms using non-paraxial light. *arXiv preprint arXiv:1403.5129*, 2014.

[40] Caleb Christensen, Sebastian Will, Michele Saba, Gyu-Boong Jo, Yong-Il Shin, Wolfgang Ketterle, and David Pritchard. Trapping of ultracold atoms in a hollow core photonic crystal fiber. *arXiv preprint arXiv:0808.0054*, 2008.

[41] J.K. Asboth and P. Domokos. Comment on „coupled dynamics of atoms and radiation-pressure-driven interferometers“ and „superstrong coupling regime of cavity quantum electrodynamics“. *Physical Review A*, 76(5):057801, 2007.

[42] Mary C. Frawley, Ivan Gusachenko, Viet Giang Truong, Marios Sergides, and Síle Nic Chormaic. Selective particle trapping and optical binding in the evanescent field of an optical nanofiber. *arXiv preprint arXiv:1403.7599*, 2014.

[43] D.E. Chang, L. Jiang, A.V. Gorshkov, and H.J. Kimble. Cavity qed with atomic mirrors. *New Journal of Physics*, 14(6):063003, 2012.